In-Phase and Opposed-Phase Imaging: Applications of Chemical Shift and Magnetic Susceptibility in the Chest and Abdomen

Anup S. Shetty, MD
Adam L. Sipe, MD
Maria Zulfiqar, MD
Richard Tsai, MD
Demetrios A. Raptis, MD
Constantine A. Raptis, MD
Sanjeev Bhalla, MD

Abbreviations: AML = angiomyolipoma, HCC = hepatocellular carcinoma, HNF-1α = hepatocyte nuclear factor 1α, LI-RADS = Liver Imaging Reporting and Data System, TE = echo time

RadioGraphics 2019; 39:115–135

https://doi.org/10.1148/rg.2019180043

Content Codes: CH GI GU MR PH

From the Mallinckrodt Institute of Radiology, Washington University School of Medicine, 510 S Kingshighway Blvd, Campus Box 8131, St Louis, MO 63110. Presented as an education exhibit at the 2017 RSNA Annual Meeting. Received March 18, 2018; revision requested May 4 and received May 14; accepted May 22. For this journal-based SA-CME activity, the authors, editor, and reviewers have disclosed no relevant relationships. **Address correspondence to** A.S.S. (e-mail: *anup.shetty@wustl.edu*).

SA-CME LEARNING OBJECTIVES

After completing this journal-based SA-CME activity, participants will be able to:

- Describe the MRI physics principles facilitating chemical shift imaging.
- Identify chemical shift signal intensity loss to make diagnoses in the chest and abdomen.
- Identify magnetic susceptibility signal intensity loss to make diagnoses in the chest and abdomen.

See rsna.org/learning-center-rg.

For the radiologist performing body MRI, chemical shift imaging is a unique tool available to investigate the cellular composition of tissue. By leveraging the inherent difference in resonant frequency between water and fat protons that is due to their local chemical environment, chemical shift image acquisition can be timed to image water and fat protons when their collective signals are in phase or out of phase, to determine the relative amount of fat signal and water signal within an individual voxel. Loss of signal intensity between the in-phase and opposed-phase MR images indicates intravoxel lipid and can be used to make definitive benign diagnoses, characterize the tissue composition of solid organs, and serve as an adjunct imaging feature aiding in the diagnosis of a variety of benign and malignant processes in the chest and abdomen. Simultaneously, T2* decay can be used to advantage at chemical shift imaging to highlight a decrease in signal intensity or amplification of signal void (blooming artifact) on longer–echo time (TE) in-phase images, compared with the shorter-TE opposed-phase images. Susceptibility-related signal intensity loss owing to T2* decay allows the identification of iron deposition, hematomas, air, metal, and melanin to aid in diagnosis.

Introduction

For MRI, pulse sequences can be used to characterize tissue composition, typically by demonstrating signal intensity differences on images obtained with sequences weighted to highlight T1 or T2 contrast, diffusion, or dynamic enhancement patterns. Chemical shift imaging offers the ability to investigate the relative ratio of fat to water content within individual voxels on an MR image. The dual gradient-echo technique for MR images offers the added benefit of highlighting T2* decay signal intensity loss related to magnetic susceptibility. This article reviews the fundamental MRI principles of chemical shift imaging and demonstrates, through representative cases, how to leverage chemical shift and magnetic susceptibility to make specific diagnoses in the chest and abdomen.

Imaging Physics

Hydrogen protons (H^+) precess at a specific frequency when placed within the magnetic field of MRI equipment. This precessional frequency is not the same for all hydrogen protons and depends on the shielding effects of the molecule's electron shell (1). As a result, water and fat protons precess at fractionally different but measurable frequencies, usually expressed as a difference of 3.5 ppm relative to the Larmor frequency of water (Fig 1). This chemical shift is directly proportional to the magnetic field strength and is approximately 225

TEACHING POINTS

- Caution should be exercised in using chemical shift signal intensity loss to diagnose adrenal adenoma in patients with a history of an HCC or renal cell carcinoma, because metastases from fat-containing variants of these neoplasms can rarely mimic the appearance of an adrenal adenoma.
- Iron deposition in the liver can mask steatosis owing to T2* decay–related signal intensity loss on the longer-TE in-phase image.
- In a patient with cirrhosis, intralesional fat is considered an ancillary feature in the 2017 guidelines of the Liver Imaging Reporting and Data System (LI-RADS), a feature which can be used to specifically favor a diagnosis of HCC over malignancy in general.
- Chemical shift imaging is a useful adjunct to other MRI sequences in differentiating between benign and malignant vertebral lesions. Most normal vertebral body bone marrow demonstrates chemical shift signal intensity loss of at least 20%.
- Gross fat will not demonstrate chemical shift signal intensity loss, and the absence of chemical shift signal intensity loss does not indicate a lack of fat—only a lack of both water and fat within a voxel.

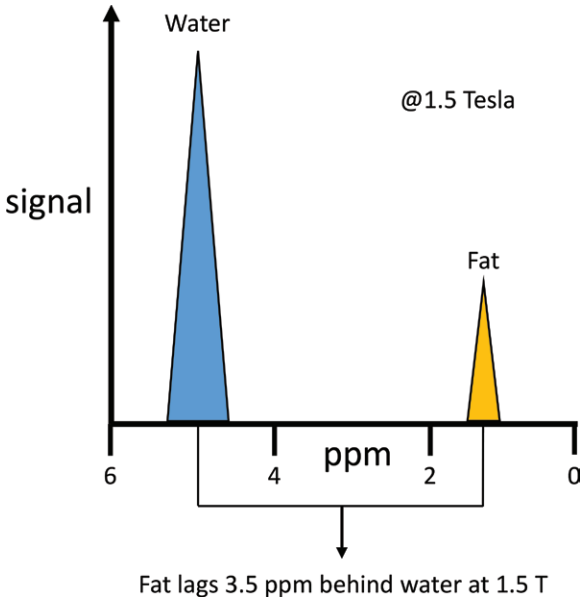

Figure 1. Chemical shift. The water signal peak (blue) and the fat signal peak (yellow) are separated at MR spectroscopy by approximately 3.5 ppm at 1.5 T.

Hz at 1.5 T and 450 Hz at 3 T. Chemical shift manifests itself at MRI in two distinct ways.

Type 1 chemical shift occurs with both spin-echo and gradient-echo imaging and is an error of spatial localization. Spatial encoding at MRI is a function of the precessional frequency, and thus the image location in the frequency-encoding direction will be slightly shifted for fat protons relative to water protons that share the same physical location. This chemical shift is proportional to the magnetic field strength and the receiver bandwidth. Higher field strengths result in greater type 1 chemical shift; a higher receiver bandwidth results in less type 1 chemical shift (Fig 2). Generally perceived as an undesirable imaging artifact, type 1 chemical shift can be mitigated by using fat-suppression techniques or by increasing receiver bandwidth.

Type 2 chemical shift, which occurs only with gradient-echo imaging, is the subtype of chemical shift that will be the subject of this article. The 180° refocusing pulse in spin-echo imaging compensates for the phase shift that occurs between water and fat protons, but gradient-echo sequences lack this pulse and are subject to type 2 chemical shift. The phase shift oscillates with a periodicity related to the inverse of the chemical shift, such that at 1.5 T, water and fat protons will be in phase at an echo time (TE) of 4.4 msec (1/225 Hz) and will be out of phase 2.2 msec before or after the first in-phase TE. Thus, voxels that contain both fat and water will have additive signal at the in-phase TE and will have cancellation of signal at the out-of-phase TE (Fig 3).

Type 2 chemical shift occurs in both the phase-encoding and the frequency-encoding directions and is maximized when the relative ratio of fat to water within a voxel is 1:1. This type 2 chemical shift is commonly seen as a sharp demarcation at the interface between organs and visceral fat or at the interface between muscle and subcutaneous fat and is referred to as the "India ink" artifact. However, smaller amounts of intravoxel fat can be detected by measuring the change in signal intensities for a region of interest between the in-phase and opposed-phase MR images. Pure fat or pure water within a voxel will result in no change in signal intensity between the in-phase and opposed-phase MR images.

An added benefit of the dual gradient-echo technique for MR images is the opportunity to assess for signal intensity loss related to magnetic susceptibility. In contradistinction to chemical shift signal intensity loss that manifests with a lower signal intensity on opposed-phase MR images, magnetic susceptibility results in signal intensity loss on in-phase MR images, because the longer TE allows more time for T2* decay to occur (2) (Fig 4). This signal intensity loss can be used to assess for sources of magnetic susceptibility in an MR image, which include paramagnetic and superparamagnetic species such as ferritin and hemosiderin, deoxyhemoglobin and extracellular methemoglobin, metals, air, calcium, and melanin (3).

If the in-phase image can be thought of as the sum of the water and fat signals for each voxel and if opposed-phase images can be thought

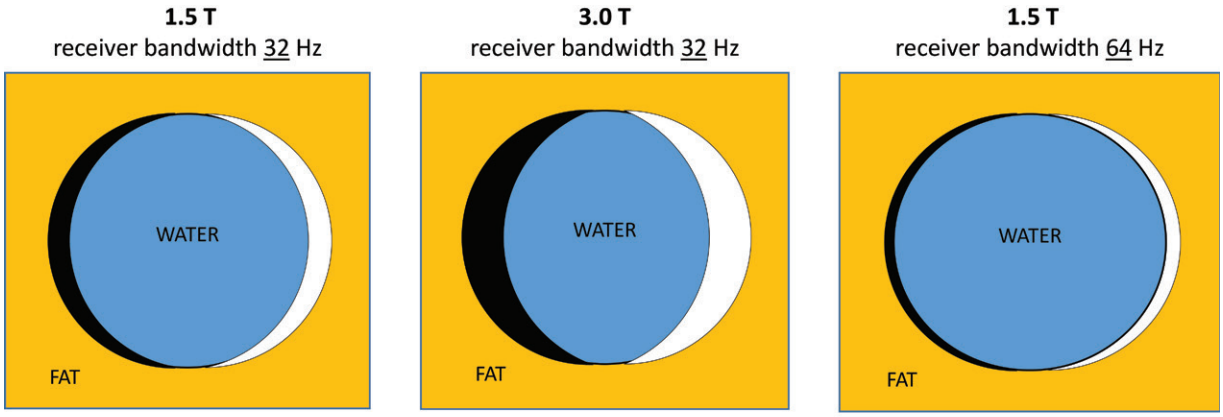

a.

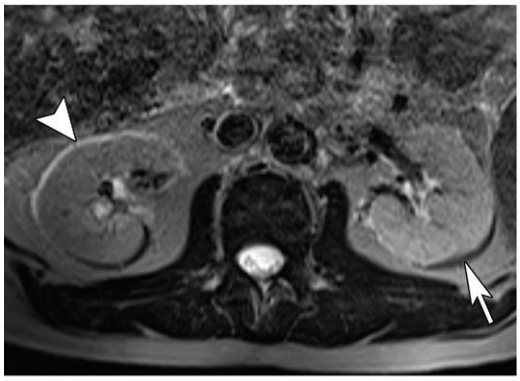

b.

Figure 2. Type 1 chemical shift. **(a)** Drawings show chemical shift with various magnetic field strengths and bandwidths. Type 1 chemical shift results in spatial misregistration of fat-containing voxels, which will not resonate at the frequency expected from a water voxel and will be mislocalized in the frequency-encoding direction at fat-water interfaces (left image). The chemical shift artifact is proportional to the magnetic field strength (larger artifact on the middle image) and is inversely proportional to the receiver bandwidth (smaller artifact on the right image). **(b)** Axial T2-weighted MR image shows a white band to the right of the interface between the right kidney and the retroperitoneal fat (arrowhead) and a dark band to the left of the interface between the left kidney and the retroperitoneal fat (arrow) as a result of type 1 chemical shift.

of as the difference between the fat and water signals, adding or subtracting the in-phase and opposed-phase images results in a water-only (fat-suppressed) or fat-only (water-suppressed) image. This method was first theorized more than 30 years ago by W. Thomas Dixon, PhD (4), and is now routinely implemented by most vendors as a fat suppression method that can be used for contrast material–enhanced fat suppression in the chest and abdomen (5,6).

Technique

The typical chemical shift MRI sequence is a T1-weighted spoiled dual gradient-echo sequence, with imaging performed either as a two- or three-dimensional acquisition. It is important to use this sequence without fat suppression to avoid masking the India ink artifact, and before the administration of intravenous gadolinium-based contrast material to avoid alterations in T1 signal intensity that may obscure chemical shift signal intensity loss. The earliest feasible out-of-phase TE is chosen to minimize signal intensity loss from T2* decay and to avoid potential confusion in the detection of iron and fat within the liver.

The in-phase and opposed-phase images should ideally be viewed simultaneously side by side, either on a single monitor or on two identically calibrated monitors to avoid artifactual differences in signal intensity. In our practice, when measuring regions of interest in the liver to assess for diffuse abnormalities, we try to avoid the center of the image in the anteroposterior plane because of the parallel imaging signal intensity loss that can occur in this region.

Quantitative measurement can be performed by carefully selecting regions of interest. The region of interest should be drawn first on the opposed-phase image to avoid measuring a region containing the India ink artifact, which would artifactually result in greater measured chemical shift signal intensity loss (7). The same region of interest should then be selected on the in-phase image, either by using the copy-and-paste function, if this function is available, or by carefully manually drawing the same region. The region of interest should encompass the region of highest signal intensity within a lesion on the in-phase image to minimize the chance of selecting a cystic or necrotic component of the lesion. In addition, correlation should be made with T2-weighted and contrast-enhanced images to avoid selecting a cystic or necrotic component.

A general search pattern for using chemical shift imaging would include *(a)* assessment of general liver signal intensity changes and identification of focal chemical shift signal intensity loss; *(b)* inspection of the adrenal glands for potential adenomas; *(c)* rapid evaluation of the spleen, pancreas, kidneys, and bone marrow; and *(d)* survey of the

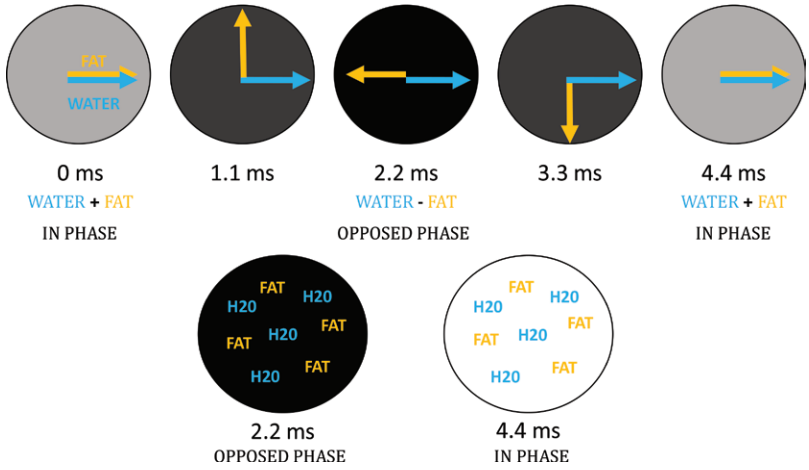

Figure 3. Type 2 chemical shift. Top row: Diagrams show that fat and water protons precess at different frequencies owing to chemical shift, such that their phases completely cancel at a TE of 2.2 msec (opposed phase) and are additive at a TE of 4.4 msec (in phase). Bottom row: Diagrams shows that if fat and water are admixed within a voxel, the voxel will lose signal intensity (chemical shift signal intensity loss) on the opposed-phase MR image, compared with the in-phase MR image.

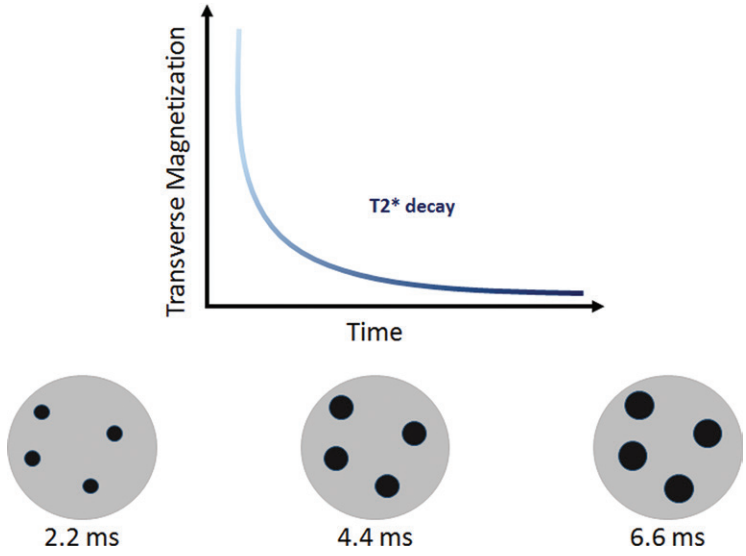

Figure 4. Magnetic susceptibility. Top: Graph shows that with a gradient-echo sequence, the lack of a 180° refocusing pulse results in irrevocable T2* decay of transverse magnetization and a resultant signal loss with time. Bottom: Diagrams of increasing TE from 2.2 msec to 6.6 msec (left to right) show that foci of susceptibility (black dots) enlarge, or "bloom," with prolonged TE because of greater T2* decay–related signal loss.

retroperitoneum, omentum, and mesentery. Use of these techniques, along with specific problem-solving applications, is discussed in the following sections (Tables 1–4).

Chemical Shift Applications

Benign Diagnosis

Adrenal Adenoma.—Adrenal adenomas are common incidental lesions, which are depicted in up to 5% of cross-sectional abdominal imaging studies (8). An adrenal mass can be characterized as an adenoma if *(a)* it visibly loses signal intensity when the in-phase and opposed-phase images are displayed with identical windows, and subtraction imaging of the in-phase image minus the opposed-phase image results in retained signal intensity within the adrenal mass; or *(b)* the signal intensity index of the adrenal mass, which is defined as 100 × [(in-phase signal intensity – opposed-phase signal intensity)/in-phase signal intensity], is greater than 16.5% (9) (Fig 5).

Most adrenal adenomas contain sufficient intracytoplasmic lipid (called "lipid-rich") to be di-

Table 1: Typical TE for In-Phase and Opposed-Phase Chemical Shift Imaging at Two Field Strengths

Sequence	TE at 1.5 T (msec)	TE at 3.0 T (msec)
First in-phase sequence	0	0
First opposed-phase sequence	2.2	1.1
Second in-phase sequence	4.4	2.2
Second opposed-phase sequence	6.6	3.3
Third in-phase sequence	8.8	4.4

Note.—The precise TE used need not be exact, but merely approximate.

Table 2: Applications of Chemical Shift Signal Intensity Loss ("Signal Dropout")

Benign diagnosis
Adrenal adenoma
Thymic hyperplasia
Renal AML (fat-poor)
Tissue characterization
Diffuse hepatic steatosis
Infiltrative or masslike hepatic steatosis
Adjunct imaging feature
Pulmonary hamartoma
Chylothorax
HCC
Hepatocellular adenoma
Hepatic AML
Xanthogranulomatous cholecystitis
Renal cell carcinoma
Retroperitoneal lymphangioma
Skeletal metastasis

Note.—AML = angiomyolipoma, HCC = hepatocellular carcinoma.

Table 3: Applications of the India Ink Artifact

Benign diagnosis
Lipomatous hypertrophy of the interatrial septum
Focal pancreatic fat
Renal AML (fat-rich)
Identification of inflammation
Acute pancreatitis
Mesenteric panniculitis
Omental infarction

agnosed at nonenhanced CT on the basis of a CT number of 10 HU or less (10). Approximately 30% of adrenal adenomas, however, are "lipid-poor" and cannot be diagnosed at nonenhanced CT, necessitating use of adrenal washout CT or chemical shift MRI to confirm the diagnosis. Multiple investigators have demonstrated that 15-minute adrenal washout CT is more accurate than chemical shift MRI for characterizing hyperattenuating adrenal adenomas, particularly if the adenoma measures more than 20–30 HU (10,11). Chemical shift MRI has a role in the diagnosis of adrenal adenomas in the 10–30-HU range at nonenhanced CT, or if the patient has a relative contraindication to CT, such as pregnancy or young age, an allergy to iodine, or renal dysfunction. Caution should be exercised in using chemical shift signal intensity loss to diagnose adrenal adenoma in patients with a history of an HCC or renal cell carcinoma, because metastases from fat-containing variants of these neoplasms can rarely mimic the appearance of an adrenal adenoma (12) (Fig 6).

Table 4: Applications of Magnetic Susceptibility ("Drop-in")

Iron deposition (liver, spleen, pancreas, kidney, marrow)
Hemorrhage
Siderotic hepatic nodules
Air (pneumobilia, pneumomediastinum, pneumatosis, pneumothorax, pneumoperitoneum)
Metal (clips, implants, devices)
Melanin

Thymic Hyperplasia.—As patients age, the thymus is gradually replaced by fat. This process has a fairly predictable but variable time course, with some patients demonstrating residual thymic tissue in the anterior mediastinum. In addition, patients may develop thymic hyperplasia in the anterior mediastinum either as a "rebound" phenomenon or in association with another disease, most commonly myasthenia gravis (13,14). In many cases, benign-appearing thymic tissue can be confidently described at CT by identifying the characteristic triangular shape of the thymus, as well as small amounts of fat within the residual or hyperplastic thymic tissue. In cases in which the radiologist cannot confidently determine benign features in the anterior mediastinal soft tissue at CT, chemical shift imaging can be used to evaluate for intravoxel lipid, which is occult at CT. Similar to adrenal adenomas, benign thymic tissue will demonstrate loss of signal intensity on opposed-phase images, and neoplastic thymic tissue will not (Fig 7).

Two methods are available for measuring the signal intensity difference between the in-phase and opposed-phase MR images (15). When using the chemical shift ratio (CSR), muscle is used as an internal control by applying the formula, $CSR = (tSI_{opp}/mSI_{opp})/(tSI_{in}/mSI_{in})$, where in = in phase, m = muscle, opp = opposed phase, SI = signal intensity, and t = thymus. Although the CSR has been found to be 100% sensitive and 96.7% specific for the detection of residual or hyperplastic thymic tissue by using a cutoff of 0.849, applying the CSR to younger patients with less intramuscular fat may lead to a loss of specificity. When dual-echo imaging is performed, the signal intensity index (SII) of the thymus is preferred because it is not dependent on the signal intensity of muscle and is calculated with the formula, $SII = [(tSI_{in} - tSI_{opp})/(tSI_{in})] \times 100\%$, where in = in phase, opp = opposed phase, SI = signal intensity, and t = thymus. Using a cutoff value of 8.92%, the SII has been shown to have a sensitivity of 100% and a specificity of 100%.

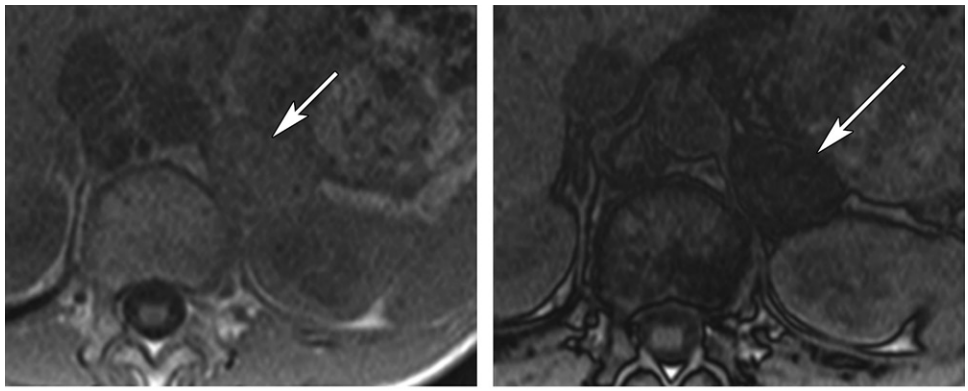

a. b.

Figure 5. Incidentally discovered adrenal mass measuring 20 HU at contrast-enhanced abdominal CT of a 70-year-old man with lung cancer. Axial T1-weighted in-phase **(a)** and opposed-phase **(b)** MR images show the mass (arrow), which demonstrates marked diffuse chemical shift signal intensity loss (arrow on **b**) on the opposed-phase image, a finding that indicates intravoxel fat and helps confirm the diagnosis of an adrenal adenoma.

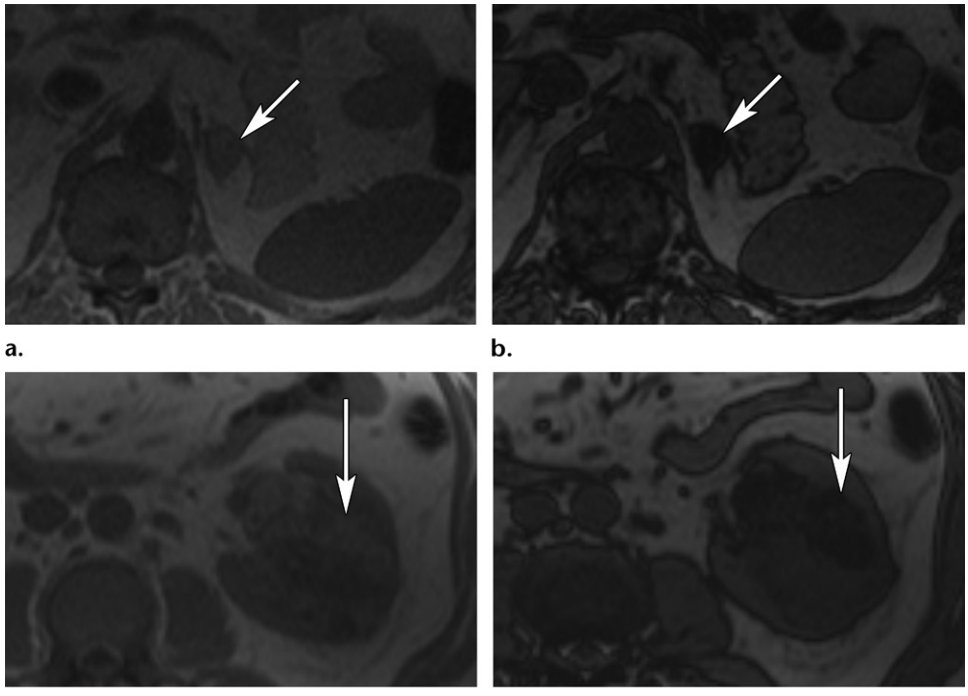

a. b.

c. d.

Figure 6. Enlarging left adrenal mass in a 64-year-old man who had undergone left nephrectomy for renal cell carcinoma (clear cell carcinoma of the kidney) 6 years earlier. **(a, b)** Axial T1-weighted in-phase **(a)** and opposed-phase **(b)** MR images show the left adrenal mass (arrow), which demonstrates marked chemical shift signal intensity loss (arrow on **b**) on the opposed-phase image, a finding that was initially suggestive of a diagnosis of adrenal adenoma. **(c, d)** Axial T1-weighted in-phase **(c)** and opposed-phase **(d)** MR images show the prior left renal mass (arrow), which demonstrates chemical shift signal intensity loss (arrow on **d**) on the opposed-phase image, a finding consistent with intravoxel fat. Thus, the left adrenal lesion is suspicious for an intravoxel fat–containing metastasis from the previous left renal cell carcinoma. The findings from histopathologic examination of the specimen from biopsy of the left adrenal mass performed at the time of cryoablation helped confirm the diagnosis of metastatic renal cell carcinoma.

Renal AML.—Renal AML belongs to the family of perivascular epithelioid cell tumors (also known as "PEComas") and contains elements of fat, smooth muscle, and blood vessels (16). Although most renal AMLs contain visible gross fat, approximately 5% of them have no visible gross fat (fat-poor AML) (17,18). Differentiating fat-poor AML from renal cell carcinoma has been the topic of considerable recent research (18–22). Although consensus is lacking, chemical shift signal intensity

Figure 7. Incidental thymic hyperplasia in a 16-year-old boy with hemoptysis, who was found to have a homogeneous anterior mediastinal mass at CT. Axial T1-weighted in-phase **(a)** and opposed-phase **(b)** MR images show the anterior mediastinal mass (arrow), which demonstrates homogeneous loss of signal intensity (arrow on **b**) on the opposed-phase image, a finding consistent with thymic hyperplasia.

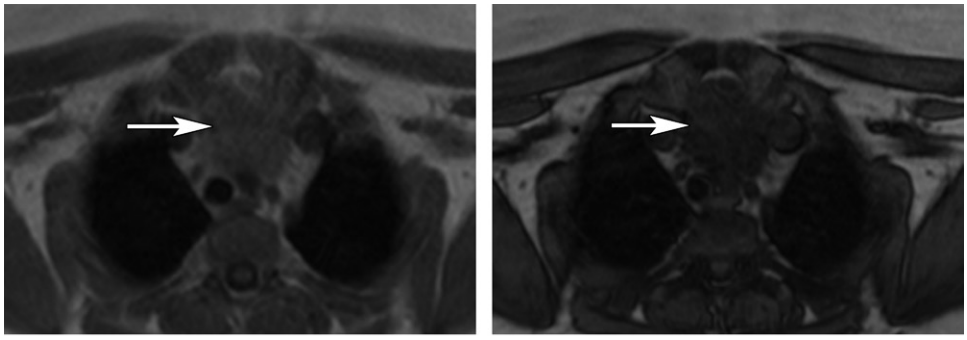

a. **b.**

Figure 8. Incidental renal mass discovered at CT in a 65-year-old woman. **(a)** Coronal T2-weighted single-shot turbo spin-echo MR image shows a T2-hypointense renal mass (arrow) in the inferior pole of the left kidney. **(b)** Axial apparent diffusion coefficient map from diffusion-weighted MRI shows marked diffusion restriction in the mass (arrow). **(c)** Axial contrast-enhanced T1-weighted fat-suppressed delayed phase MR image shows less enhancement of the mass (arrow) than that of normal kidney. Features from these images are suspicious for a renal malignancy such as a papillary renal cell carcinoma. **(d, e)** Axial T1-weighted in-phase **(d)** and opposed-phase **(e)** MR images show the mass (arrow), which demonstrates marked chemical shift signal intensity loss (arrow on **e**) on the opposed-phase image, a finding that is suggestive of a lipid-poor AML. The results of histopathologic examination of the specimen obtained at biopsy helped confirm the diagnosis of a lipid-poor AML.

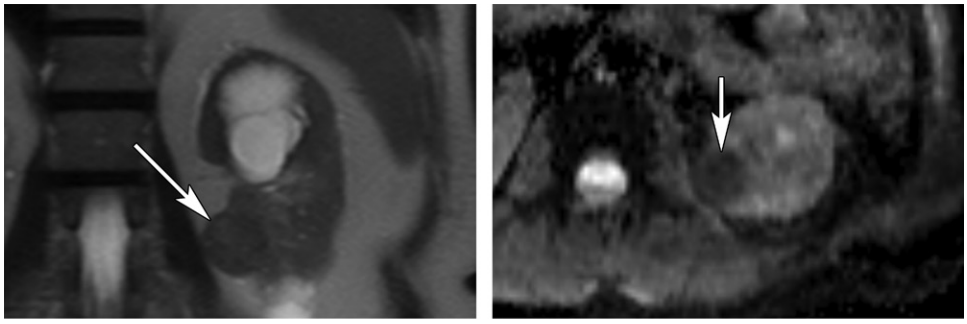

a. **b.**

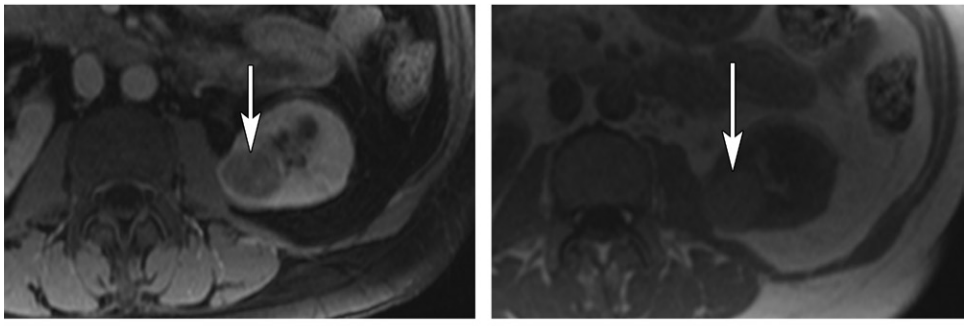

c. **d.**

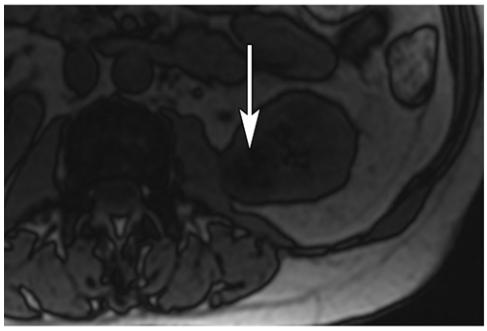

e.

loss may have value in suggesting the potential for a diagnosis of fat-poor AML (Fig 8), along with small size, homogeneous hyperattenuation on nonenhanced CT images, T2 hypointensity, homogeneous enhancement at MRI, lack of necrosis, lack of hemorrhage, and a lower apparent diffusion coefficient. However, because of the overlap in the imaging features of fat-poor AML with the imaging features of papillary renal cell carcinoma, in

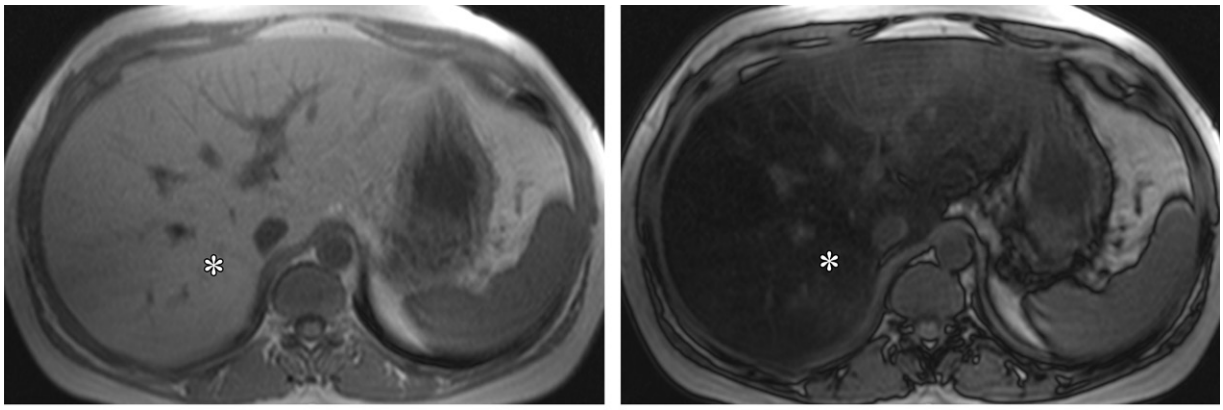

a. b.

Figure 9. Diffuse hepatic steatosis in a 39-year-old woman with recurrent pancreatitis. Axial T1-weighted in-phase **(a)** and opposed-phase **(b)** MR images show an area of the liver (*) that demonstrates diffuse chemical shift signal intensity loss (* on **b**) on the opposed-phase image, a finding consistent with diffuse hepatic steatosis.

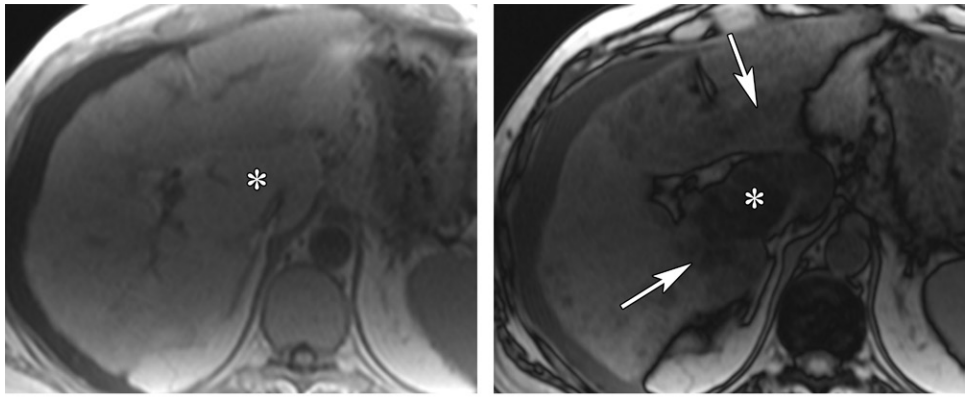

a. b.

Figure 10. Abdominal distention in a 44-year-old man with abnormal results of liver function tests and a remote history of testicular cancer. The initial CT findings were suspicious for liver masses. Axial T1-weighted in-phase **(a)** and opposed-phase **(b)** MR images show the enlarged caudate lobe (*), which demonstrates marked chemical shift signal intensity loss (* on **b**), as well as more nodular infiltrative signal intensity loss in the right and left hepatic lobes (arrows on **b**), on the opposed-phase image, findings consistent with masslike and infiltrative hepatic steatosis. The findings at histopathologic examination of the specimen from liver biopsy helped confirm the diagnosis of hepatic steatosis.

our practice we typically recommend biopsy of the renal mass to establish a definitive diagnosis before contemplating ablation or resection.

Tissue Characterization

A primary application of abdominal MRI is the detection and quantification of hepatic steatosis. Hepatic steatosis results from a complex interplay of hormones, nutrition, and genetics and is defined by accumulation of more than 5% fat in the liver (23). Chemical shift imaging is now used routinely to separate the water and fat signal fractions, allowing detection of fat fractions of more than 10%–15% (24).

Diffuse hepatic steatosis is typically diagnosed with chemical shift imaging by identifying diffuse chemical shift signal intensity loss on the opposed-phase MR image (Fig 9), but certain caveats should be recognized. Iron deposition in the liver can mask steatosis owing to T2* decay–related signal intensity loss on the longer-TE in-phase image. This method can be used to detect fat fractions only up to 50%, beyond which the opposed-phase signal intensity begins to increase again because of the ambiguity of fat or water signal dominance with dual-echo chemical shift. If more quantitative and accurate measurements of the fat fraction are desired, a proton-density fat fraction can be calculated, typically by using a gradient-echo technique with six echoes of progressively longer TEs. Infiltrative, focal, or masslike hepatic steatosis presents a more interesting diagnostic dilemma that can be solved with chemical shift imaging (Fig 10).

Adjunct Imaging Feature

Changes in chemical shift signal intensity, apart from being used to make specific diagnoses, can

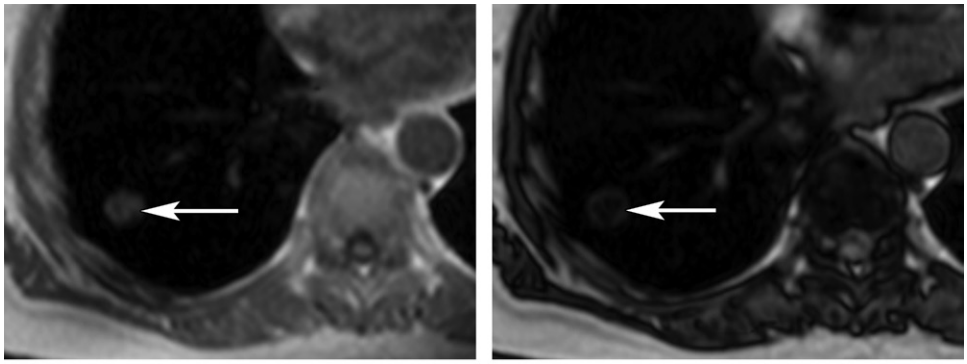

a. b.

Figure 11. Incidental pulmonary hamartoma in a 67-year-old woman with metastatic appendiceal cancer. Axial T1-weighted in-phase **(a)** and opposed-phase **(b)** MR images show a right lower lobe pulmonary nodule (arrow), which demonstrates marked chemical shift signal intensity loss (arrow on **b**) on the opposed-phase image, a finding consistent with a pulmonary hamartoma.

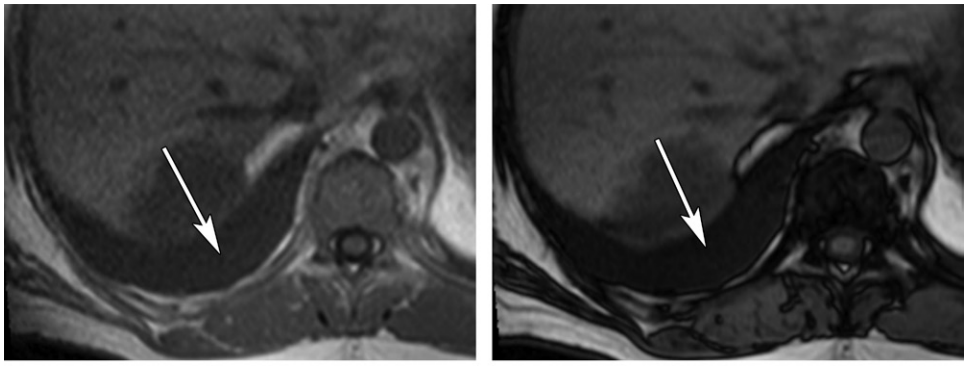

a. b.

Figure 12. Spontaneous chylothorax in a 52-year-old man presenting after an insect bite to the left side of the neck. Axial T1-weighted in-phase **(a)** and opposed-phase **(b)** MR images show the right-sided pleural effusion (arrow), which demonstrates chemical shift signal intensity loss (arrow on **b**) on the opposed-phase image, a finding that is consistent with intravoxel water and fat within the pleural effusion and is suggestive of a chylothorax. The results of pleural fluid analysis demonstrated a triglyceride level of more than 4425 mg/dL, a finding consistent with chylothorax.

also be used as an adjunct feature to suggest a diagnosis or guide further imaging and management. In the chest, the diagnosis of a pulmonary hamartoma, which is a benign mesenchymal neoplasm containing variable amounts of fat, cartilage, smooth muscle, and epithelial elements (25), can be suggested at chemical shift imaging by the finding of a chemical shift ratio of 0.45 or less when characteristic calcification and fat are not present at CT (26), which is the case more than half of the time (27) (Fig 11). The diagnosis of chylothorax, a pleural effusion composed of lymphatic fluid occurring either spontaneously, in the posttraumatic setting, or after esophagectomy or lung resection (28), can be suggested when chemical signal intensity loss that is due to fat and water within the pleural effusion is demonstrated (Fig 12).

In the liver, HCC is the most common primary hepatic malignancy; and in most recent practice guidelines, image-based diagnosis is preferred to biopsy for diagnosis (29). In a patient with cirrhosis, intralesional fat is considered an ancillary feature in the 2017 guidelines of the Liver Imaging Reporting and Data System (LI-RADS), a feature which can be used to specifically favor a diagnosis of HCC over malignancy in general (Fig 13). Fat is more common in well-differentiated or moderately differentiated HCC (30). When fat is found (up to 20% of the time, particularly in smaller masses), the pattern is more typically diffuse in smaller lesions and patchy in larger lesions (31,32).

Hepatocellular adenoma, a benign liver neoplasm, may also contain intravoxel fat, particularly the hepatocyte nuclear factor 1α (HNF-1α)–mutated subtype of hepatocellular adenoma (33) (Fig 14). Chronic liver disease, the demographics of the patient, and the dynamic enhancement pattern are helpful factors for distinguishing between HCC and hepatocellular adenoma. In our practice, chemical shift signal intensity loss in a liver mass that is suspected to represent an

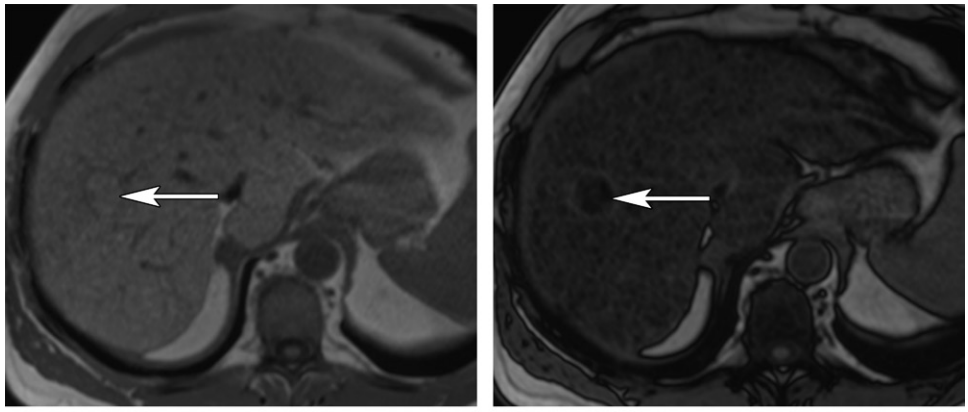

a. b.

Figure 13. Alcoholic cirrhosis in a 56-year-old man. Axial T1-weighted in-phase **(a)** and opposed-phase **(b)** MR images show a liver mass (arrow), which demonstrates chemical shift signal intensity loss (arrow on **b**) on the opposed-phase image, a finding consistent with intravoxel fat, which is a LI-RADS ancillary feature favoring a diagnosis of HCC in particular. The findings at histopathologic examination of the specimen obtained at biopsy helped confirm HCC.

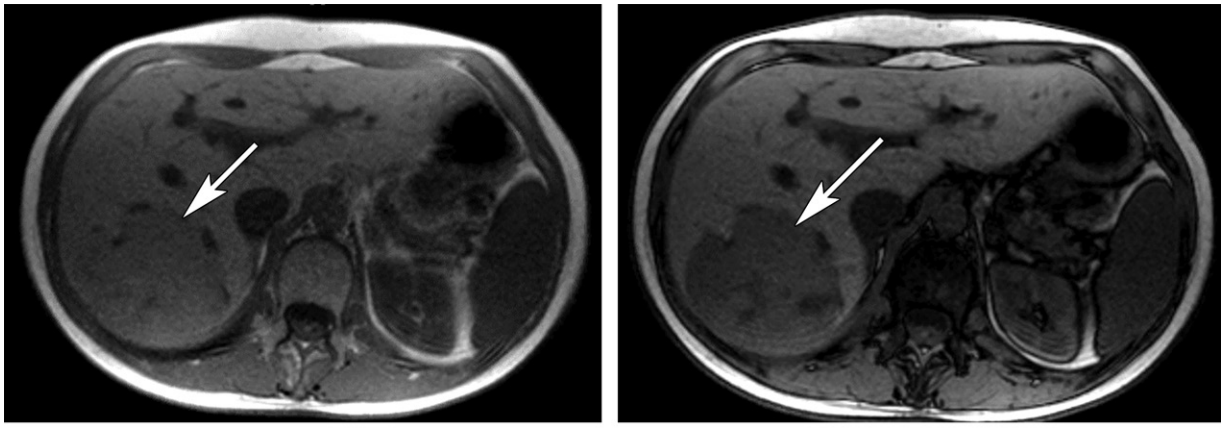

a. b.

Figure 14. HNF-1α–mutated hepatocellular adenoma in a 35-year-old woman with a history of hysterectomy who was receiving hormone replacement therapy with a transdermal estrogen patch. T1-weighted in-phase **(a)** and opposed-phase **(b)** MR images show the lesion (arrow), which demonstrates homogeneous chemical shift signal intensity loss (arrow on **b**) on the opposed-phase image. The demographics of the patient, her history, and the absence of chronic liver disease allowed a confident diagnosis of HNF-1α–mutated hepatocellular adenoma.

adenoma will prompt our hepatology and surgical colleagues to delay liver biopsy until cessation of oral contraceptive therapy or weight loss can be undertaken, because HNF-1α–mutated hepatocellular adenomas are more common in women receiving oral contraceptive therapy and may shrink with the previous interventions.

Finally, hepatic AML, like renal AML, may contain gross fat, intravoxel fat, or both (Fig 15). A female patient demographic (34) and a history of tuberous sclerosis complex (35) may be helpful factors that are suggestive of the diagnosis, but hepatic AML is sufficiently rare that biopsy is usually required for diagnosis.

Xanthogranulomatous cholecystitis is an unusual form of chronic cholecystitis in which lipid-laden macrophages deposit in the wall of the gallbladder (36), resulting in inflammation of the gallbladder and adjacent structures and potentially overlapping in appearance with adenocarcinoma of the gallbladder (37). Chemical shift signal intensity loss in the thickened wall of the gallbladder has been described in the setting of xanthogranulomatous cholecystitis and can be used to help favor the diagnosis of xanthogranulomatous cholecystitis over gallbladder cancer (38) (Fig 16), although histologic confirmation is required.

Retroperitoneal lymphangiomas are uncommon benign cystic masses containing variable amounts of chyle (39). Chemical shift signal intensity loss has been proposed as a potential tool to differentiate lymphangiomas from other mesenteric or retroperitoneal cystic lesions. In the findings from a study of 24 patients with mesenteric and retroperitoneal cysts, investigators found that approximately a third of cases demonstrated intravoxel fat

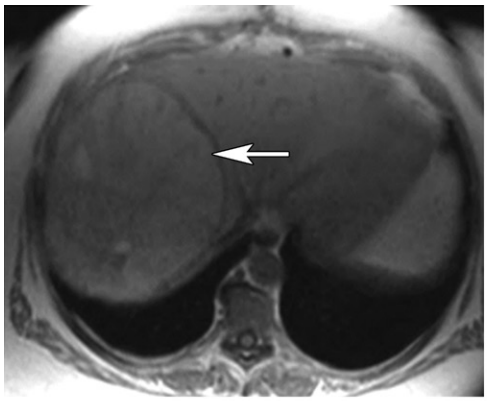

Figure 15. Incidentally discovered hepatic AML in a 45-year-old woman. **(a, b)** Axial T1-weighted in-phase **(a)** and opposed-phase **(b)** MR images show a large right hepatic lobe mass (arrow), which demonstrates heterogeneous chemical shift signal intensity loss (arrow on **b**) on the opposed-phase image, a finding consistent with foci of intravoxel lipid. **(c)** Axial contrast-enhanced T1-weighted fat-suppressed MR image shows washout of the mass and foci of gross fat (arrow) within the mass, manifested by signal intensity loss with fat suppression.

a.

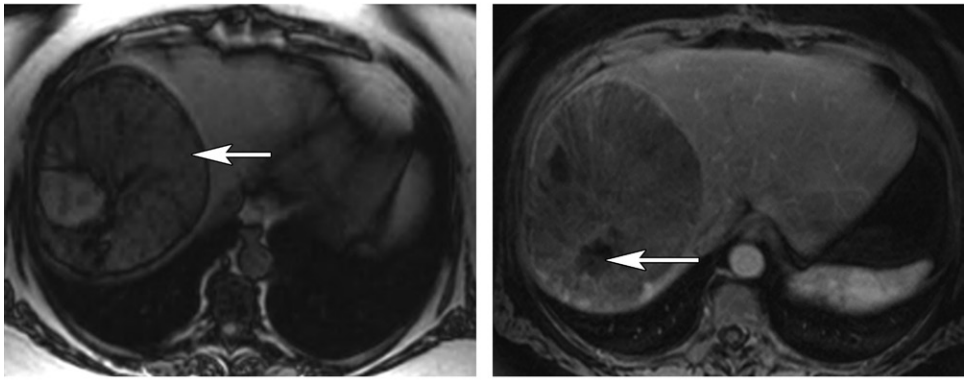

b. **c.**

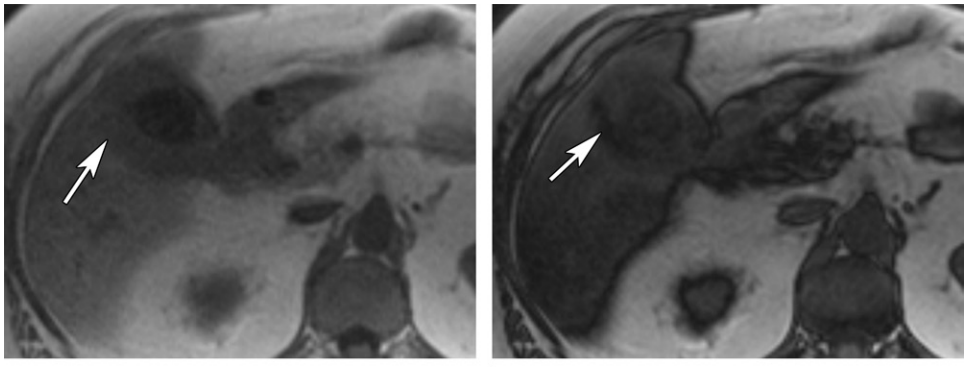

a. **b.**

Figure 16. Xanthogranulomatous cholecystitis in a 62-year-old man with long-standing gallbladder wall thickening. Axial T1-weighted in-phase **(a)** and opposed-phase **(b)** MR images show the thickened gallbladder wall (arrow), which demonstrates focal chemical shift signal intensity loss (arrow on **b**) on the opposed-phase image, a finding consistent with intravoxel fat.

(40) (Fig 17). Assessment for chemical shift signal intensity loss is a rapid and easy method to allow the potential for a more specific imaging diagnosis.

Evaluation of the spine is a critical but occasionally overlooked task at body MRI. Chemical shift imaging is a useful adjunct to other MRI sequences in differentiating between benign and malignant vertebral lesions. Most normal vertebral body bone marrow demonstrates chemical shift signal intensity loss of at least 20% (41). Multiple groups of investigators have demonstrated the potential value of chemical shift imaging in distinguishing malignant lesions from benign lesions of the spine (42–45), because malignant lesions demonstrate little to no chemical shift signal intensity loss (Fig 18).

India Ink Applications

Lipomatous hypertrophy of the interatrial septum is characterized by excess deposition of unencapsulated adipose tissue in the interatrial septum, typically sparing the fossa ovalis, with a dumbbell configuration (46,47). Not infrequently, lipomatous hypertrophy of the

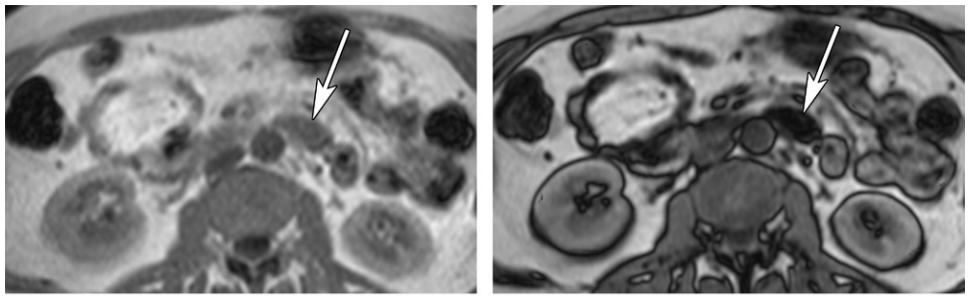

a. b.

Figure 17. Incidental left para-aortic lesion measuring –9 HU at CT in a 47-year-old woman with a pelvic smooth muscle tumor of unknown malignant potential. Axial T1-weighted in-phase **(a)** and opposed-phase **(b)** MR images show the left para-aortic lesion (arrow), which demonstrates marked internal chemical shift signal intensity loss (arrow on **b**) on the opposed-phase image, a finding consistent with a combination of intravoxel water and fat. Axial contrast-enhanced T1-weighted fat-suppressed MR images (not shown) demonstrated no enhancement, a finding consistent with a retroperitoneal lymphangioma.

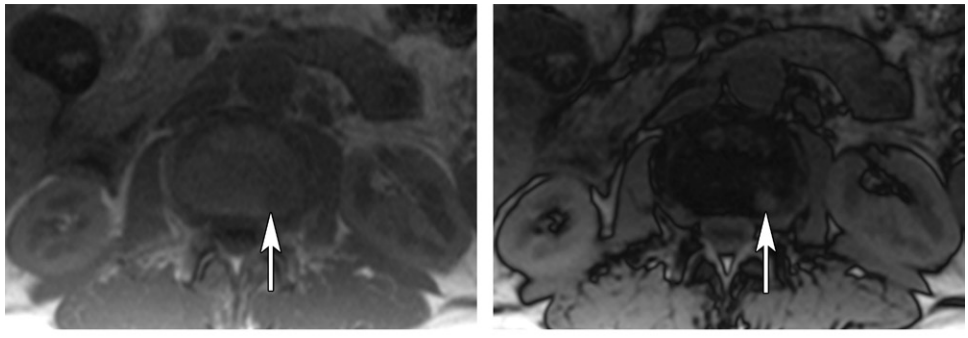

a. b.

Figure 18. L3 vertebral body lesion in a 59-year-old man with HCC. Axial T1-weighted in-phase **(a)** and opposed-phase **(b)** MR images show the lesion (arrow), which demonstrates an absence of chemical shift signal intensity loss within the lesion (arrow on **b**) on the opposed-phase image. MR images obtained with other sequences (not shown) demonstrated T2 hyperintensity, diffusion restriction, and enhancement, findings consistent with metastatic HCC.

interatrial septum can be mistaken for a mass at echocardiography, triggering further imaging workup. Frequently, a diagnosis can be made at CT with findings of nonenhancing, unencapsulated fat deposition with a described characteristic dumbbell shape and location. In challenging or atypical cases, MRI can be used to confirm the fatty nature and lack of enhancement of lipomatous hypertrophy of the interatrial septum and may be performed as the next diagnostic study after the initial echocardiography. Chemical shift imaging can help to confirm gross fat through the India ink artifact at the interface between the atrium and the fat-containing interatrial septum (Fig 19). Note that lipomatous hypertrophy may be entirely macroscopic fat and thus not demonstrate signal intensity dropout on in-phase and opposed-phase images. In these cases, fat-saturated MR images should be used to help confirm macroscopic fat.

The India ink artifact can also be used to detect focal pancreatic fat. Focal fat deposition can simulate a subtle, infiltrative pancreatic ductal adenocarcinoma and can be distinguished by the India ink artifact at chemical shift imaging, which would not be expected with a true intrapancreatic mass that has no intrapancreatic fat-water interface (Fig 20). The India ink artifact can also be used to detect pancreatic lipomas (48).

Fat-rich renal AML, although detectable at abdominal MRI by using fat-suppression techniques (49), may sometimes be easier to detect at chemical shift imaging, especially if the AML is small. The gross fat within the lesion will produce an India ink artifact at interfaces with kidney; and in our practice, we find the India ink artifact particularly useful for identifying exophytic lesions with homogeneous signal intensity that may be challenging to distinguish from adjacent perinephric fat (Fig 21).

The India ink artifact can also be helpful in the detection of small amounts of water admixed with retroperitoneal or mesenteric fat, such as in acute pancreatitis or mesenteric panniculitis, or the detection of subtle encapsulation of fatty inflammation, such as in an omental infarct.

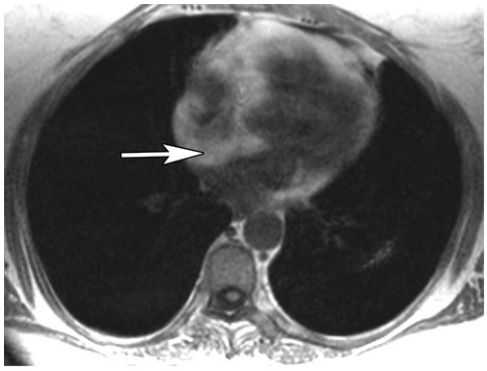

a.

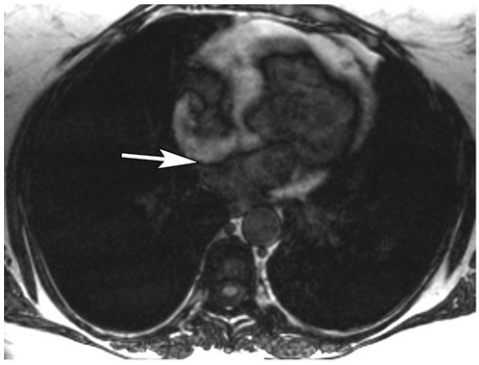

b.

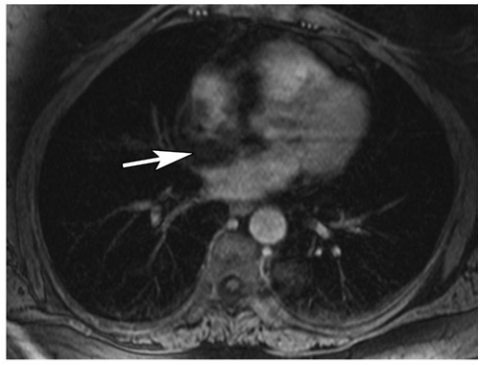

c.

Figure 19. Incidental lipomatous hypertrophy of the interatrial septum in a 61-year-old man with lung cancer. **(a, b)** Axial T1-weighted in-phase **(a)** and opposed-phase **(b)** MR images show T1-hyperintense material (arrow) within the interatrial septum, with an India ink artifact at the interface with the left atrium (arrow on **b**) on the opposed-phase image, a finding that helps confirm a fat-water interface. **(c)** Axial contrast-enhanced T1-weighted fat-suppressed MR image shows suppression of signal intensity in the atrial septum with no enhancement (arrow), findings consistent with lipomatous hypertrophy of the interatrial septum.

a.

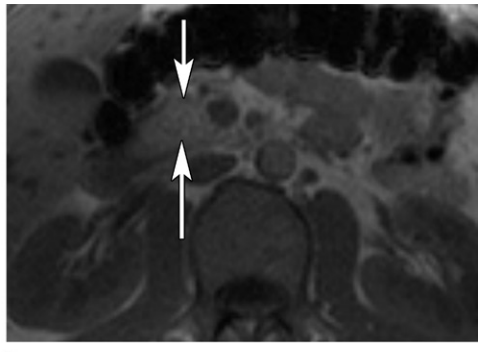

b.

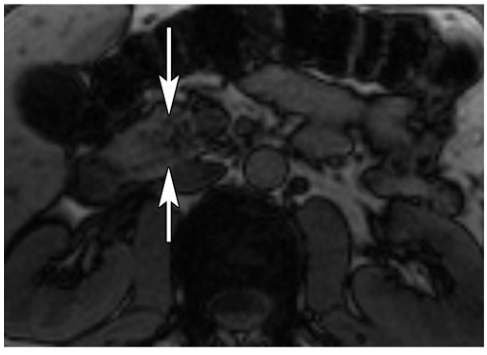

c.

Figure 20. Pancreatic lesion in a 25-year-old man presenting with abdominal pain. **(a)** Axial contrast-enhanced CT image shows an ill-defined hypoattenuating lesion (arrows) in the pancreatic head. **(b, c)** Axial T1-weighted in-phase **(b)** and opposed-phase **(c)** MR images show stippled chemical shift signal intensity loss (arrows) in the area corresponding to the hypoattenuating lesion on **a**, findings that are consistent with intravoxel fat and focal intrapancreatic fat deposition.

Magnetic Susceptibility Applications

Heme

In chronic hematomas, iron atoms agglutinate into large metalloprotein complexes along the walls of the cavity of the hematoma, forming ferritin and hemosiderin, which are superparamagnetic and induce marked T2*-related signal intensity loss (50). The in-phase image is typically acquired after the opposed-phase image to ensure that chemical shift signal intensity loss is discernible from magnetic susceptibility signal intensity loss. Thus, in-phase imaging with its longer TE demonstrates "blooming" or accentuation of the

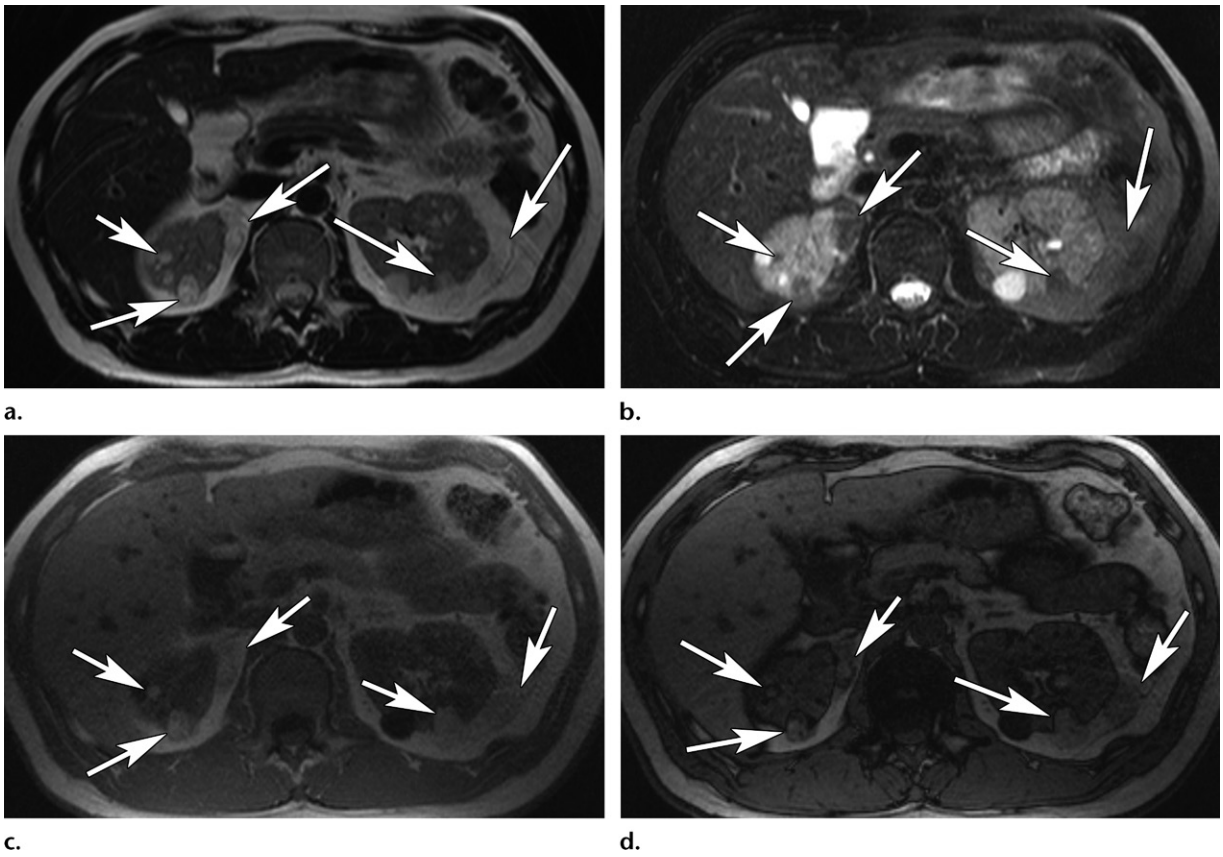

Figure 21. Bilateral renal AMLs in a 40-year-old man with tuberous sclerosis complex. **(a)** Axial T2-weighted turbo spin-echo MR image shows multiple T2-hyperintense masses (arrows) within both kidneys. **(b)** Axial T2-weighted turbo spin-echo fat-suppressed MR image shows signal intensity loss within each of the identified lesions (arrows), a finding that indicates gross fat and helps confirm the diagnosis of renal AMLs. **(c, d)** Axial T1-weighted in-phase **(c)** and opposed-phase **(d)** MR images show that for each of the lesions (arrows), an India ink artifact is depicted at the interface of the lesions with the kidney, a finding that helps confirm the diagnosis of renal AMLs. Heterogeneous chemical shift signal intensity loss in the exophytic renal lesions increases their conspicuity compared with their appearance on the fat-suppressed T2-weighted MR image in **b**.

hypointense rim from blood products, particularly hemosiderin, in a hematoma (Fig 22) or hemorrhagic cyst (Fig 23) and can aid in making the specific diagnosis.

Iron in the human body is predominantly found in the functional forms of hemoglobin and myoglobin, with approximately 20% of the iron stored as ferritin, primarily in the reticuloendothelial system of the liver, spleen, and bone marrow (51). Pathologic iron deposition occurs in the setting of increased absorption from the gastrointestinal tract in patients with hereditary hemochromatosis, in patients undergoing long-term blood transfusion therapy with resultant secondary hemosiderosis, and in patients with chronic liver disease. Iron deposition can be identified qualitatively at chemical shift imaging by magnetic susceptibility–related signal intensity loss on the longer TE in-phase images or can be assessed both more sensitively and quantitatively by using a multigradient-echo technique with an empirically derived relationship between the calculated relaxation parameter R2* and the liver iron concentration (52,53). The pattern of iron deposition within the thoracoabdominal organs is helpful in distinguishing hemochromatosis from hemosiderosis, because extrahepatic reticuloendothelial deposition in the spleen and bone marrow occurs more frequently with hemosiderosis (Fig 24) and is a late finding in hemochromatosis. Iron deposition in the pancreas and the heart is typical in hemochromatosis (Fig 25) but not in hemosiderosis.

Regenerative siderotic nodules are intracellular iron-containing nodules typically found in the cirrhotic liver (54). Magnetic susceptibility can be used to sensitively identify these lesions (55,56) (Fig 25b). The relatively small time difference in TE between the opposed-phase and in-phase sequences may not highlight siderotic nodules to their maximal effect; and in our practice, the multigradient-echo sequence that we use for liver iron quantification is also used to accentuate the blooming of siderotic nodules at longer TEs.

Air

Molecular oxygen within the air, unlike oxygen dissolved in tissue, is slightly paramagnetic compared with most tissue in the body (57).

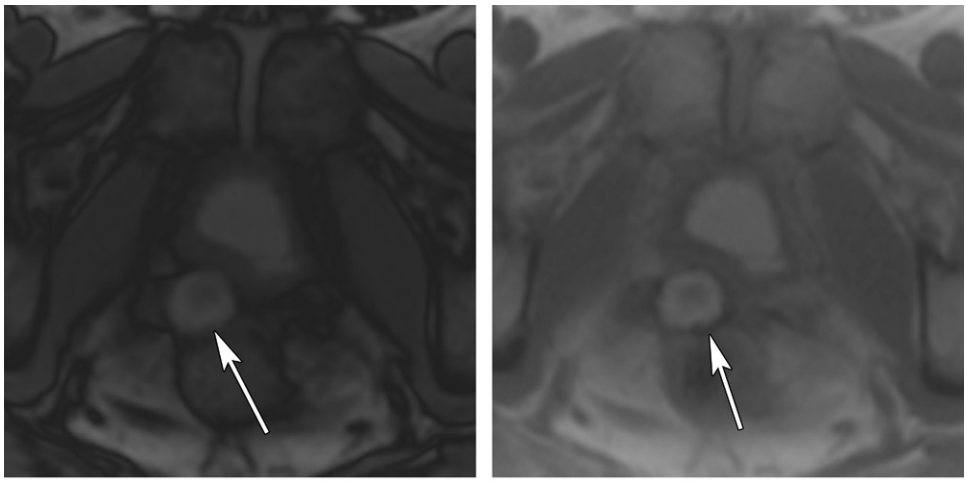

a. b.

Figure 22. Mass in the rectovesical space detected at evaluation before brachytherapy seed placement in a 71-year-old man who had previously undergone prostatectomy for prostate cancer. Axial T1-weighted opposed-phase **(a)** and in-phase **(b)** MR images show the peripheral hypointense rim of an intrinsically T1-hyperintense lesion (arrow), which demonstrates magnetic susceptibility signal intensity loss (arrow on **b**) on the in-phase image, a finding consistent with hemosiderin deposition. Contrast-enhanced fat-suppressed T1-weighted subtraction MRI (not shown) helped confirm the absence of enhancement, which was consistent with the diagnosis of a hematoma after prostatectomy.

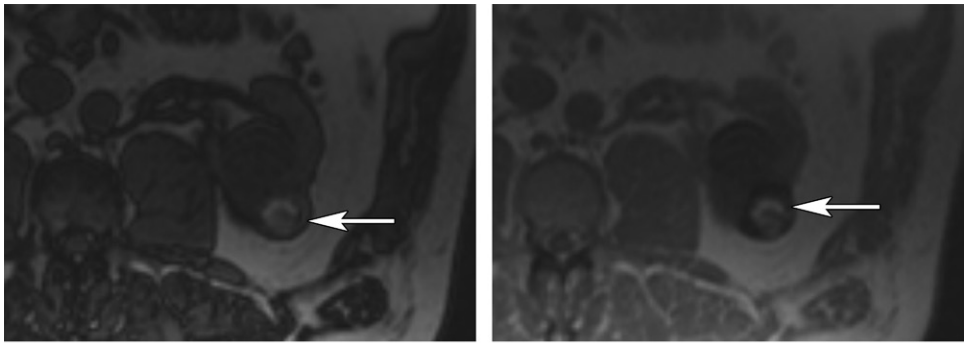

a. b.

Figure 23. Incidental left renal lesion measuring approximately 35 HU at nonenhanced abdominal CT in a 60-year-old man with prostate cancer. Axial T1-weighted opposed-phase **(a)** and in-phase **(b)** MR images show the left renal lesion (arrow), which demonstrates central T1 hyperintensity consistent with blood products, as well as magnetic susceptibility signal intensity loss (arrow on **b**) in the periphery of the lesion, a finding consistent with hemosiderin, on the in-phase image. Contrast-enhanced MRI (not shown) demonstrated no enhancement at subtraction imaging, which helped confirm the diagnosis of a hemorrhagic renal cyst.

Susceptibility artifact that results from gradient-echo imaging with longer TEs can be exploited at MRI to identify subtle foci of air that would be trivial to diagnose at CT. Pneumobilia, or gas within the biliary tree, is important to recognize at MRI, particularly at MR cholangiopancreatography, because pneumobilia may mimic hepatolithiasis or choledocholithiasis (58). Utilizing chemical shift sequences to assess for blooming artifact on the longer-TE in-phase MR images that is due to magnetic susceptibility is substantially more accurate than relying on T2-weighted MR cholangiopancreatographic images alone to distinguish pneumobilia from a biliary stone (Fig 26).

In a similar fashion, pneumomediastinum, the presence of air within the mediastinum, and pneumatosis intestinalis, the presence of air within the bowel, can be detected by using magnetic susceptibility signal intensity loss at chemical shift imaging (Fig 27). Air in a pneumothorax or pneumoperitoneum could theoretically also be better detected on in-phase images if the volume of air is small enough to highlight blooming artifact, although practically speaking, large volumes of air will usually be readily detectable at T2-weighted MRI.

Metal

Susceptibility artifact from metallic clips, implants, and devices is frequently a major

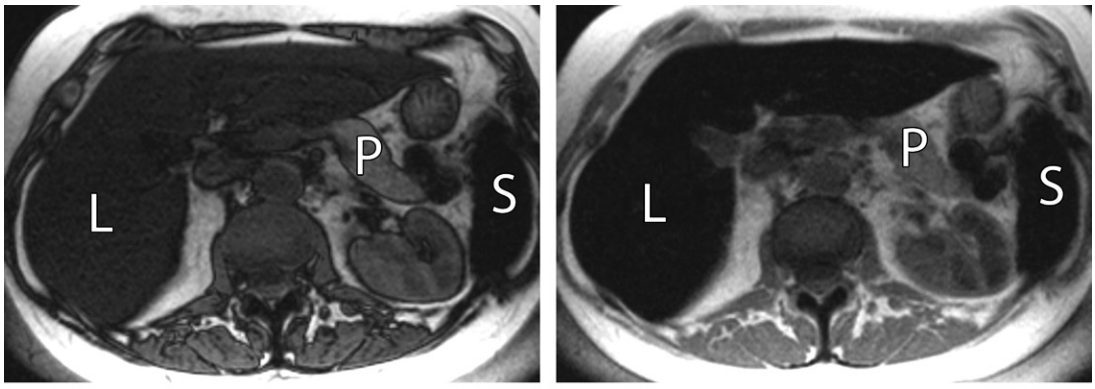

a. **b.**

Figure 24. Hemosiderosis pattern of iron deposition in a 71-year-old woman with chronic anemia who was being treated with blood transfusions. Axial T1-weighted opposed-phase **(a)** and in-phase **(b)** MR images show magnetic susceptibility signal intensity loss within the liver *(L)* on the longer-TE in-phase image in **b**, marked hypointensity of the spleen *(S)* on both the in-phase and opposed-phase images, and no signal intensity loss in the pancreas *(P)*, findings consistent with a hemosiderosis pattern of reticuloendothelial iron deposition.

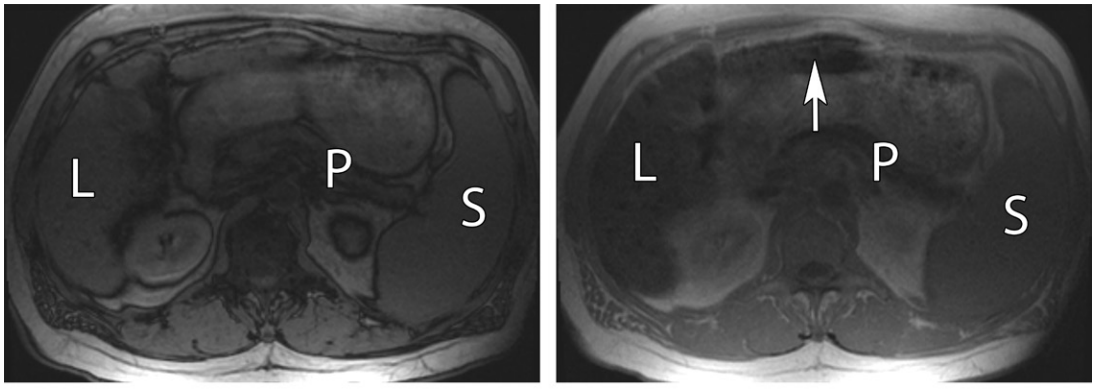

a. **b.**

Figure 25. Hemochromatosis and siderotic nodules in a 56-year-old man. Axial T1-weighted opposed-phase **(a)** and in-phase **(b)** MR images show magnetic susceptibility signal intensity loss in the liver *(L)* and pancreas *(P)* on the in-phase image, without the same degree of signal intensity loss in the spleen *(S)*, findings consistent with a primary hemochromatosis pattern of iron deposition. Siderotic hepatic nodules (arrow on **b**) are also more conspicuous on the longer-TE in-phase image.

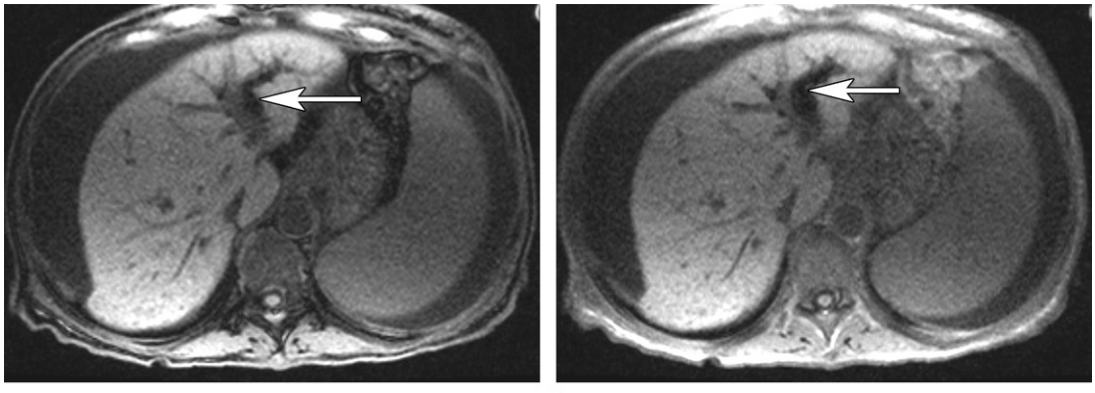

a. **b.**

Figure 26. Pneumobilia in a 57-year-old woman with metastatic pancreatic cancer. Axial T1-weighted opposed-phase **(a)** and in-phase **(b)** MR images show an area of linear T1 hypointensity in the left hepatic duct (arrow), which demonstrates blooming of the hypointense area (arrow on **b**) on the longer-TE in-phase image, a finding consistent with pneumobilia.

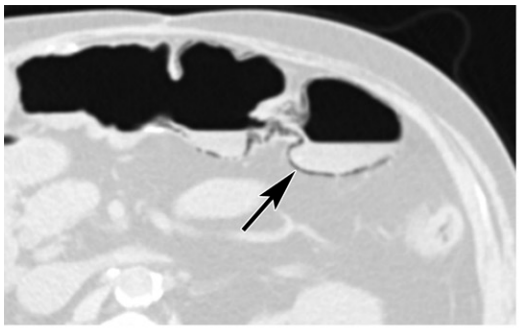

Figure 27. Pneumatosis intestinalis in a 55-year-old man with HCC and abdominal pain. **(a)** Axial nonenhanced abdominal CT image (lung windows) shows pneumatosis intestinalis (arrow) in the transverse colon. **(b, c)** Axial T1-weighted opposed-phase **(b)** and in-phase **(c)** MR images show foci of magnetic susceptibility in the wall of the transverse colon (arrow), which demonstrate blooming (arrow on **c**) on the longer-TE in-phase image, a finding consistent with gas and pneumatosis intestinalis. Note that the India ink artifact will be present at the interface between the colon and mesenteric fat on opposed-phase images, and this artifact should not be mistaken for pneumatosis.

a.

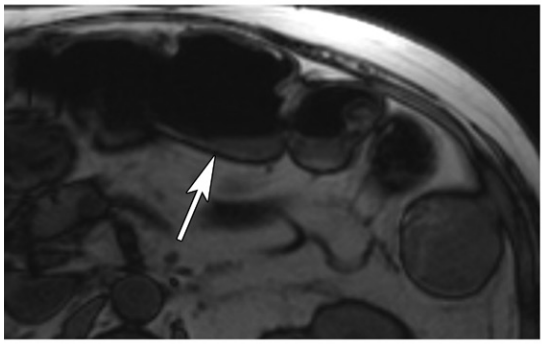

b.

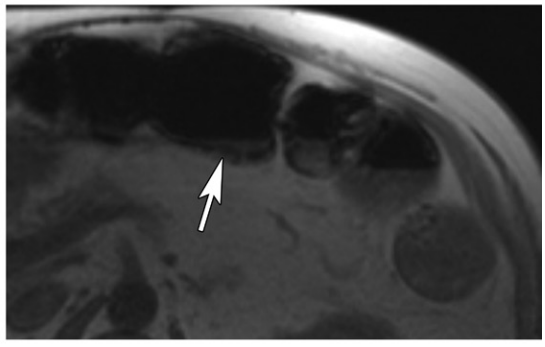

c.

challenge at MRI. Metallic ions range in susceptibility from weakly paramagnetic, such as gadolinium ions in the blood or trace metal ions present in the body such as copper or manganese, to moderately paramagnetic, such as titanium, to ferromagnetic, such as stainless steel or pure iron (57). Distortions of the magnetic field result in T2* decay–related signal intensity loss and alterations in the resonant frequency of adjacent structures, which can impair fat saturation, reduce the accuracy of spatial localization, and alter geometric depiction (59). Metal artifact reduction with novel MRI sequences is of considerable interest to facilitate the evaluation of joints or other anatomic structures, such as the prostate gland, that might otherwise be obscured by artifact from a prosthesis (60).

It would be reasonable to question why one would want to accentuate metallic susceptibility artifact, but for the person performing body MRI, susceptibility can be a useful tool for identifying surgical material that might otherwise go unnoticed. Small metallic clips can be obscured with single-shot turbo spin-echo MRI and with rapid gradient-echo MRI with short TEs. The chemical shift sequence therefore offers the ability to identify subtle surgical material with confidence (61), for example, cholecystectomy clips (Fig 28). We have observed in our practice that subtle or tiny amounts of surgical material, such as a dropped clip serving as a nidus for inflammation, are often easier to identify at chemical shift imaging than at CT.

Melanin

Melanotic melanoma is well known for its T1 hyperintensity, primarily a function of scavenging of paramagnetic metal species such as manganese, copper, and zinc (62). An additional contributor to both T1 hyperintensity and T2 hypointensity is the propensity for metastatic melanoma to hemorrhage, with resultant deoxyhemoglobin and methemoglobin creating additional paramagnetic susceptibility effects (63). T1 hyperintensity in metastatic melanoma to the liver, although highly characteristic, occurs in only 20%–50% of cases (64). Particularly in patients with background steatosis, chemical shift imaging will reveal T1-hyperintense metastatic lesions that retain signal intensity on opposed-phase images (Fig 29).

Pitfalls

Gross fat will not demonstrate chemical shift signal intensity loss, and the absence of chemical shift signal intensity loss does not indicate a lack of fat—only a lack of both water and fat within a voxel. Careful assessment of non–fat-suppressed and fat-suppressed MR images, in conjunction with chemical shift imaging, is necessary to completely exclude fat within a lesion, for example, in an adrenal myelolipoma (Fig 30). Caution should also be exercised in the spine with predominantly fatty processes such as Modic type 2 endplate changes or radiation-induced fatty marrow replacement (65).

Care should be taken with the interpretation of small lesions, in which the India ink artifact may

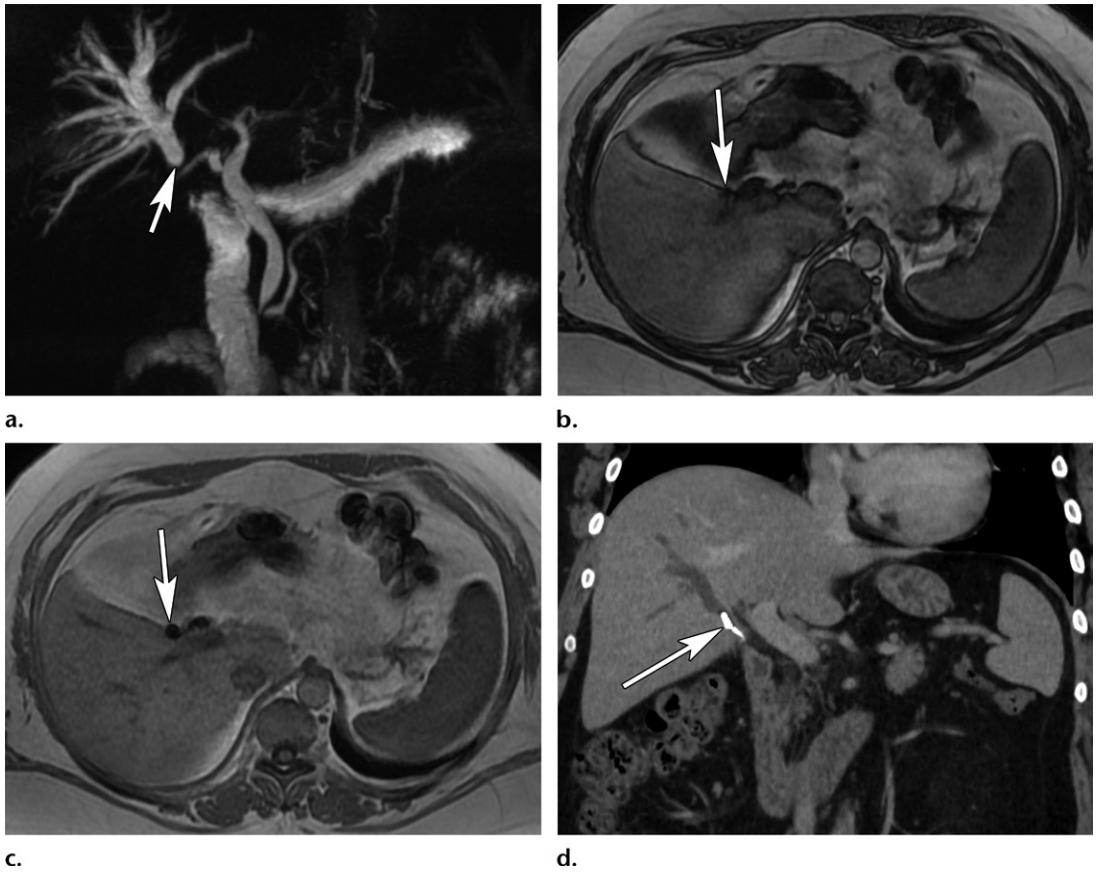

Figure 28. Intrahepatic biliary ductal dilatation in a 37-year-old woman after cholecystectomy. **(a)** Coronal three-dimensional MR cholangiopancreatographic maximum intensity projection image shows focal dilatation of the right anterior hepatic ductal system, with an abrupt cutoff (arrow). **(b, c)** Axial T1-weighted opposed-phase **(b)** and in-phase **(c)** MR images show the site of the ductal cutoff (arrow), which demonstrates blooming artifact (arrow on **c**) that is more apparent on the longer-TE in-phase image. **(d)** Coronal contrast-enhanced abdominal CT image shows surgical clips (arrow) at the site of the excluded duct in liver segment 8.

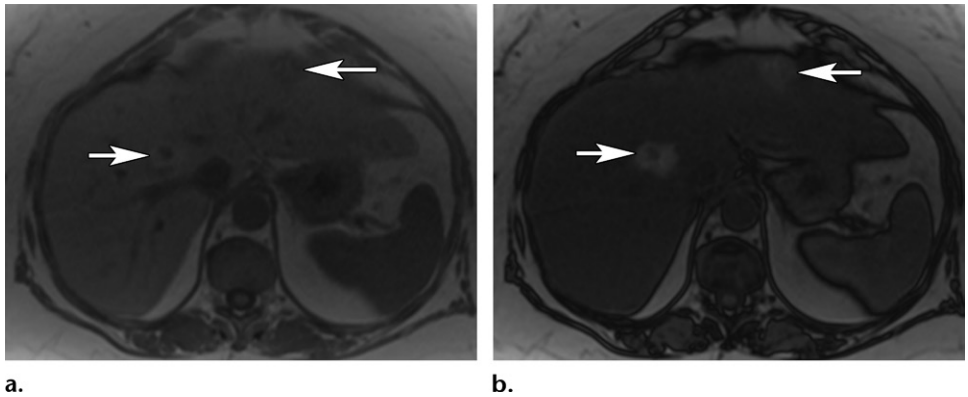

Figure 29. New suspicious liver lesions found at CT in a 58-year-old woman with metastatic melanoma. Axial T1-weighted in-phase **(a)** and opposed-phase **(b)** MR images show T1-hyperintense liver lesions (arrows), which become far more apparent (arrows on **b**) with background liver signal intensity loss from diffuse hepatic steatosis on the opposed-phase image, a finding consistent with metastatic melanoma.

constitute the majority of the lesion depicted on the opposed-phase image and could lead to an erroneous diagnosis of intravoxel lipid, for example, in diagnosing an adrenal adenoma (9). Necrotic lesions may also mimic chemical shift signal intensity loss because of the potential for multiple fat-water interfaces within a lesion creating an India ink artifact and artifactual signal intensity loss on opposed-phase images, and necrotic lesions should be evaluated with contrast-enhanced imaging.

Magnetic susceptibility–related signal intensity loss, although more conspicuous on longer-TE

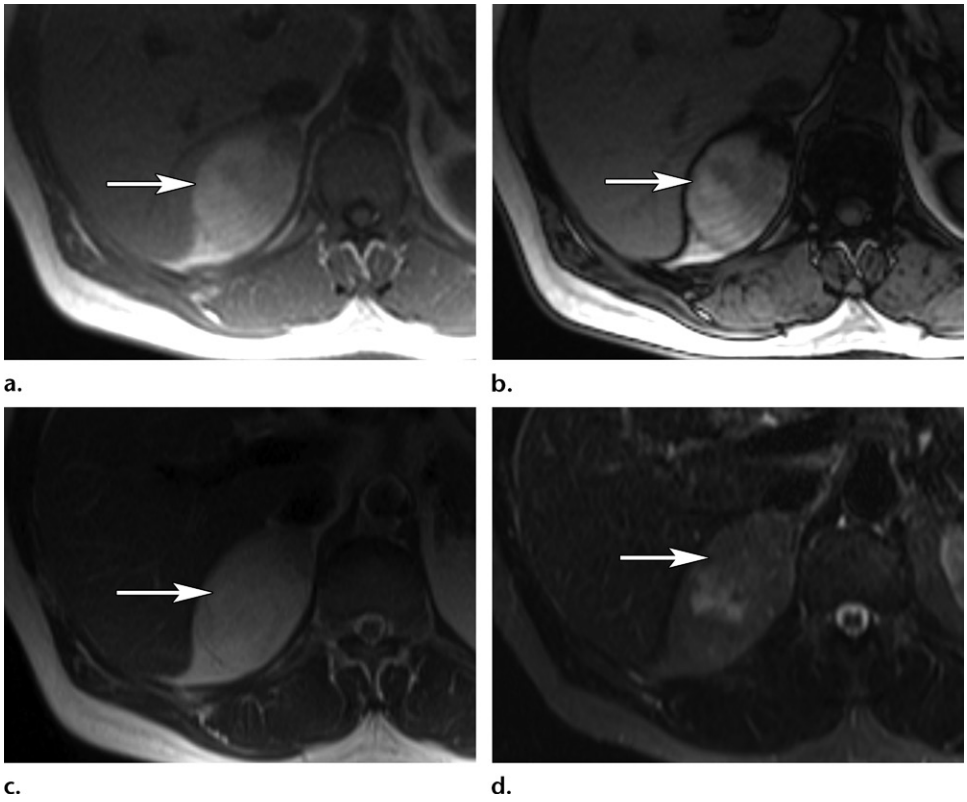

Figure 30. Incidental right adrenal mass in a 55-year-old man. **(a, b)** Axial T1-weighted in-phase **(a)** and opposed-phase **(b)** MR images show no signal intensity loss within the right adrenal mass (arrow). Note that an India ink artifact (arrow on **b**) is depicted between the liver and the mass on the opposed-phase image, a finding that indicates a fat-water interface. **(c, d)** Axial T2-weighted MR images obtained without **(c)** and with **(d)** fat suppression show that the mass (arrow) demonstrates marked signal intensity loss with fat suppression (arrow on **d**), a finding consistent with gross fat and a diagnosis of adrenal myelolipoma.

in-phase images, compared with opposed-phase images, may be too subtle to recognize if it is small in magnitude. The inclusion of a multigradient-echo sequence with progressively longer TE with each echo, although typically used for liver iron and fat quantification, can also be used to greatly increase the conspicuity of susceptibility-related signal intensity loss.

If chemical shift water-fat separation with the Dixon method is used for fat suppression, the limitations of this technique should be recognized (66). Local fat-water swap can occur because of the ambiguity of separating the water and fat signals owing to phase error. A smoother transition between adequate and poor fat suppression, known as a leakage of fat into water signal or vice versa, can occur because of eddy currents. Modern Dixon-based methods such as the three-point technique attempt to mitigate these artifacts and provide a generally robust fat-suppression method.

Finally, if you are performing chemical shift imaging at 3 T, the periodicity of in-phase and opposed-phase TEs is half the length of that at 1.5 T, such that the first in-phase TE is 2.2 msec, rather than 4.4 msec. Most newer models of 3-T MRI equipment are capable of capturing the first opposed-phase echo at 1.1 msec, but if this is not the case and the opposed-phase image is obtained after the in-phase image, magnetic susceptibility–related signal intensity loss should be sought on the opposed-phase images, compared with the in-phase images, rather than vice versa. Hepatic signal intensity loss on the longer-TE opposed-phase images then becomes difficult to parse into chemical shift signal intensity loss or magnetic susceptibility signal intensity loss.

Conclusion

Chemical shift imaging is used routinely at body MRI, with wide-ranging applications. Detection of intravoxel fat and delineation of fat-water interfaces can be used throughout the chest and abdomen for problem solving beyond the capabilities of conventional MRI and CT. Magnetic susceptibility highlighted by T2* signal intensity decay on longer-TE in-phase images can be used to detect hemorrhage, iron deposition, pathologic air, metallic surgical material, and melanin.

Knowledge of how to optimally use chemical shift imaging will increase the speed and utility with which the person performing body MRI approaches a familiar sequence.

References

1. Hood MN, Ho VB, Smirniotopoulos JG, Szumowski J. Chemical shift: the artifact and clinical tool revisited. RadioGraphics 1999;19(2):357–371.
2. Chavhan GB, Babyn PS, Thomas B, Shroff MM, Haacke EM. Principles, techniques, and applications of T2*-based MR imaging and its special applications. RadioGraphics 2009;29(5):1433–1449.
3. Tsushima Y, Endo K. Hypointensities in the brain on T2*-weighted gradient-echo magnetic resonance imaging. Curr Probl Diagn Radiol 2006;35(4):140–150.
4. Dixon WT. Simple proton spectroscopic imaging. Radiology 1984;153(1):189–194.
5. Takatsu Y, Akasaka T, Miyati T. The Dixon technique and the frequency-selective fat suppression technique in three-dimensional T1 weighted MRI of the liver: a comparison of contrast-to-noise ratios of hepatocellular carcinomas-to-liver. Br J Radiol 2015;88(1050):20150117. https://www.birpublications.org/doi/pdf/10.1259/bjr.20150117. Published May 8, 2015.
6. Kishida Y, Koyama H, Seki S, et al. Comparison of fat suppression capability for chest MR imaging with Dixon, SPAIR and STIR techniques at 3 Tesla MR system. Magn Reson Imaging 2018;47:89–96.
7. Raptis CA, McWilliams SR, Ratkowski KL, Broncano J, Green DB, Bhalla S. Mediastinal and pleural MR imaging: practical approach for daily practice. RadioGraphics 2018;38(1):37–55.
8. Schieda N, Siegelman ES. Update on CT and MRI of adrenal nodules. AJR Am J Roentgenol 2017;208(6):1206–1217.
9. Siegelman ES. Adrenal MRI: techniques and clinical applications. J Magn Reson Imaging 2012;36(2):272–285.
10. Seo JM, Park BK, Park SY, Kim CK. Characterization of lipid-poor adrenal adenoma: chemical-shift MRI and washout CT. AJR Am J Roentgenol 2014;202(5):1043–1050.
11. Haider MA, Ghai S, Jhaveri K, Lockwood G. Chemical shift MR imaging of hyperattenuating (>10 HU) adrenal masses: does it still have a role? Radiology 2004;231(3):711–716.
12. Schieda N, Al Dandan O, Kielar AZ, Flood TA, McInnes MD, Siegelman ES. Pitfalls of adrenal imaging with chemical shift MRI. Clin Radiol 2014;69(11):1186–1197.
13. Araki T, Sholl LM, Gerbaudo VH, Hatabu H, Nishino M. Imaging characteristics of pathologically proven thymic hyperplasia: identifying features that can differentiate true from lymphoid hyperplasia. AJR Am J Roentgenol 2014;202(3):471–478.
14. Priola AM, Priola SM. Imaging of thymus in myasthenia gravis: from thymic hyperplasia to thymic tumor. Clin Radiol 2014;69(5):e230–e245. https://www.clinicalradiologyonline.net/article/S0009-9260(14)00028-2/fulltext. Published February 26, 2014.
15. Priola AM, Priola SM, Ciccone G, et al. Differentiation of rebound and lymphoid thymic hyperplasia from anterior mediastinal tumors with dual-echo chemical-shift MR imaging in adulthood: reliability of the chemical-shift ratio and signal intensity index. Radiology 2015;274(1):238–249.
16. Lim RS, Flood TA, McInnes MDF, Lavallee LT, Schieda N. Renal angiomyolipoma without visible fat: can we make the diagnosis using CT and MRI? Eur Radiol 2018;28(2):542–553.
17. Park BK. Renal angiomyolipoma: radiologic classification and imaging features according to the amount of fat. AJR Am J Roentgenol 2017;209(4):826–835.
18. Sasiwimonphan K, Takahashi N, Leibovich BC, Carter RE, Atwell TD, Kawashima A. Small (<4 cm) renal mass: differentiation of angiomyolipoma without visible fat from renal cell carcinoma utilizing MR imaging. Radiology 2012;263(1):160–168. [Published correction appears in Radiology 2016;280(2):653.]
19. Potretzke AM, Potretzke TA, Bauman TM, et al. Computed tomography and magnetic resonance findings of fat-poor angiomyolipomas. J Endourol 2017;31(2):119–128.
20. Woo S, Kim SY, Cho JY, Kim SH. Differentiation between papillary renal cell carcinoma and fat-poor angiomyolipoma: a preliminary study assessing detection of intratumoral hemorrhage with chemical shift MRI and T2*-weighted gradient echo. Acta Radiol 2018;59(5):627–634.
21. Chen LS, Zhu ZQ, Wang ZT, et al. Chemical shift magnetic resonance imaging for distinguishing minimal-fat angiomyolipoma from renal cell carcinoma: a meta-analysis. Eur Radiol 2018;28(5):1854–1861.
22. Ding Y, Zeng M, Rao S, Chen C, Fu C, Zhou J. Comparison of biexponential and monoexponential model of diffusion-weighted imaging for distinguishing between common renal cell carcinoma and fat poor angiomyolipoma. Korean J Radiol 2016;17(6):853–863.
23. Pappachan JM, Babu S, Krishnan B, Ravindran NC. Non-alcoholic fatty liver disease: a clinical update. J Clin Transl Hepatol 2017;5(4):384–393.
24. Hong CW, Fazeli Dehkordy S, Hooker JC, Hamilton G, Sirlin CB. Fat quantification in the abdomen. Top Magn Reson Imaging 2017;26(6):221–227.
25. Meyer CA, White CS. Cartilaginous disorders of the chest. RadioGraphics 1998;18(5):1109–1123; quiz 1241–1242.
26. Hochhegger B, Marchiori E, dos Reis DQ, et al. Chemical-shift MRI of pulmonary hamartomas: initial experience using a modified technique to assess nodule fat. AJR Am J Roentgenol 2012;199(3):W331–W334.
27. Park KY, Kim SJ, Noh TW, et al. Diagnostic efficacy and characteristic feature of MRI in pulmonary hamartoma: comparison with CT, specimen MRI, and pathology. J Comput Assist Tomogr 2008;32(6):919–925.
28. Platis IE, Nwogu CE. Chylothorax. Thorac Surg Clin 2006;16(3):209–214.
29. Elsayes KM, Hooker JC, Agrons MM, et al. 2017 version of LI-RADS for CT and MR imaging: an update. RadioGraphics 2017;37(7):1994–2017.
30. Costa AF, Thipphavong S, Arnason T, Stueck AE, Clarke SE. Fat-containing liver lesions on imaging: detection and differential diagnosis. AJR Am J Roentgenol 2018;210(1):68–77.
31. Kutami R, Nakashima Y, Nakashima O, Shiota K, Kojiro M. Pathomorphologic study on the mechanism of fatty change in small hepatocellular carcinoma of humans. J Hepatol 2000;33(2):282–289.
32. Prasad SR, Wang H, Rosas H, et al. Fat-containing lesions of the liver: radiologic-pathologic correlation. RadioGraphics 2005;25(2):321–331.
33. Katabathina VS, Menias CO, Shanbhogue AK, Jagirdar J, Paspulati RM, Prasad SR. Genetics and imaging of hepatocellular adenomas: 2011 update. RadioGraphics 2011;31(6):1529–1543.
34. Lee SJ, Kim SY, Kim KW, et al. Hepatic angiomyolipoma versus hepatocellular carcinoma in the noncirrhotic liver on gadoxetic acid-enhanced MRI: a diagnostic challenge. AJR Am J Roentgenol 2016;207(3):562–570.
35. O'Malley ME, Chawla TP, Lavelle LP, Cleary S, Fischer S. Primary perivascular epithelioid cell tumors of the liver: CT/MRI findings and clinical outcomes. Abdom Radiol (NY) 2017;42(6):1705–1712.
36. Singh VP, Rajesh S, Bihari C, Desai SN, Pargewar SS, Arora A. Xanthogranulomatous cholecystitis: what every radiologist should know. World J Radiol 2016;8(2):183–191.
37. Zhao F, Lu PX, Yan SX, et al. CT and MR features of xanthogranulomatous cholecystitis: an analysis of consecutive 49 cases. Eur J Radiol 2013;82(9):1391–1397.
38. Hatakenaka M, Adachi T, Matsuyama A, Mori M, Yoshikawa Y. Xanthogranulomatous cholecystitis: importance of chemical-shift gradient-echo MR imaging. Eur Radiol 2003;13(9):2233–2235.
39. Rajiah P, Sinha R, Cuevas C, Dubinsky TJ, Bush WH Jr, Kolokythas O. Imaging of uncommon retroperitoneal masses. RadioGraphics 2011;31(4):949–976.
40. Ayyappan AP, Jhaveri KS, Haider MA. Radiological assessment of mesenteric and retroperitoneal cysts in adults: is there a role for chemical shift MRI? Clin Imaging 2011;35(2):127–132.

41. Zajick DC Jr, Morrison WB, Schweitzer ME, Parellada JA, Carrino JA. Benign and malignant processes: normal values and differentiation with chemical shift MR imaging in vertebral marrow. Radiology 2005;237(2):590–596.
42. Shi YJ, Li XT, Zhang XY, Liu YL, Tang L, Sun YS. Differential diagnosis of hemangiomas from spinal osteolytic metastases using 3.0 T MRI: comparison of T1-weighted imaging, chemical-shift imaging, diffusion-weighted and contrast-enhanced imaging. Oncotarget 2017;8(41): 71095–71104.
43. Douis H, Davies AM, Jeys L, Sian P. Chemical shift MRI can aid in the diagnosis of indeterminate skeletal lesions of the spine. Eur Radiol 2016;26(4):932–940.
44. El-Samie HA, El-Ghany HS. The value of added opposed/in phase MRI sequences in characterization of the focal vertebral bone marrow lesions in oncology patients. Egypt J Radiol Nucl Med 2015;46(3):727–732.
45. Geith T, Schmidt G, Biffar A, et al. Comparison of qualitative and quantitative evaluation of diffusion-weighted MRI and chemical-shift imaging in the differentiation of benign and malignant vertebral body fractures. AJR Am J Roentgenol 2012;199(5):1083–1092.
46. Kimura F, Matsuo Y, Nakajima T, et al. Myocardial fat at cardiac imaging: how can we differentiate pathologic from physiologic fatty infiltration? RadioGraphics 2010;30(6): 1587–1602.
47. Gaerte SC, Meyer CA, Winer-Muram HT, Tarver RD, Conces DJ Jr. Fat-containing lesions of the chest. RadioGraphics 2002;22(Spec Issue):S61–S78.
48. Manning MA, Srivastava A, Paal EE, Gould CF, Mortele KJ. Nonepithelial neoplasms of the pancreas: radiologic-pathologic correlation, part 1—benign tumors. RadioGraphics 2016;36(1):123–141.
49. Jinzaki M, Silverman SG, Akita H, Mikami S, Oya M. Diagnosis of renal angiomyolipomas: classic, fat-poor, and epithelioid types. Semin Ultrasound CT MR 2017;38(1):37–46.
50. Bradley WG Jr. MR appearance of hemorrhage in the brain. Radiology 1993;189(1):15–26.
51. Hernando D, Levin YS, Sirlin CB, Reeder SB. Quantification of liver iron with MRI: state of the art and remaining challenges. J Magn Reson Imaging 2014;40(5):1003–1021.
52. Hernando D, Cook RJ, Diamond C, Reeder SB. Magnetic susceptibility as a B_0 field strength independent MRI biomarker of liver iron overload. Magn Reson Med 2013;70(3):648–656.
53. Sarigianni M, Liakos A, Vlachaki E, et al. Accuracy of magnetic resonance imaging in diagnosis of liver iron overload: a systematic review and meta-analysis. Clin Gastroenterol Hepatol 2015;13(1):55–63.e5.
54. Curvo-Semedo L, Brito JB, Seco MF, Costa JF, Marques CB, Caseiro-Alves F. The hypointense liver lesion on T2-weighted MR images and what it means. RadioGraphics 2010;30(1):e38. https://pubs.rsna.org/doi/10.1148/rg.e38. Published January 1, 2010.
55. Dai Y, Zeng M, Li R, et al. Improving detection of siderotic nodules in cirrhotic liver with a multi-breath-hold susceptibility-weighted imaging technique. J Magn Reson Imaging 2011;34(2):318–325.
56. Li RK, Zeng MS, Qiang JW, et al. Improving detection of iron deposition in cirrhotic liver using susceptibility-weighted imaging with emphasis on histopathological correlation. J Comput Assist Tomogr 2017;41(1):18–24.
57. Schenck JF. The role of magnetic susceptibility in magnetic resonance imaging: MRI magnetic compatibility of the first and second kinds. Med Phys 1996;23(6):815–850.
58. Erden A, Haliloğlu N, Genç Y, Erden I. Diagnostic value of T1-weighted gradient-echo in-phase images added to MRCP in differentiation of hepatolithiasis and intrahepatic pneumobilia. AJR Am J Roentgenol 2014;202(1):74–82.
59. Hargreaves BA, Worters PW, Pauly KB, Pauly JM, Koch KM, Gold GE. Metal-induced artifacts in MRI. AJR Am J Roentgenol 2011;197(3):547–555.
60. Talbot BS, Weinberg EP. MR imaging with metal-suppression sequences for evaluation of total joint arthroplasty. RadioGraphics 2016;36(1):209–225.
61. Merkle EM, Nelson RC. Dual gradient-echo in-phase and opposed-phase hepatic MR imaging: a useful tool for evaluating more than fatty infiltration or fatty sparing. RadioGraphics 2006;26(5):1409–1418.
62. Enochs WS, Petherick P, Bogdanova A, Mohr U, Weissleder R. Paramagnetic metal scavenging by melanin: MR imaging. Radiology 1997;204(2):417–423.
63. Gaviani P, Mullins ME, Braga TA, et al. Improved detection of metastatic melanoma by T2*-weighted imaging. AJNR Am J Neuroradiol 2006;27(3):605–608.
64. Balasubramanya R, Selvarajan SK, Cox M, et al. Imaging of ocular melanoma metastasis. Br J Radiol 2016;89(1065): 20160092.
65. Tadros MY, Louka AL. Discrimination between benign and malignant in vertebral marrow lesions with diffusion weighted MRI and chemical shift. Egypt J Radiol Nucl Med 2016;47(2):557–569.
66. Eggers H, Börnert P. Chemical shift encoding-based water-fat separation methods. J Magn Reson Imaging 2014;40(2): 251–268.